MOUNTAIN-PLAINS CONSORTIUM

MPC 23-511 | C.P. Pantelides and D. Tran

DURABLE BRIDGES USING GLASS FIBER REINFORCED POLYMER AND HYBRID REINFORCED CONCRETE COLUMNS

MOUNTAIN-PLAINS CONSORTIUM REGION 8

A University Transportation Center sponsored by the U.S. Department of Transportation serving the Mountain-Plains Region. Consortium members:

Colorado State University
North Dakota State University
South Dakota State University
University of Colorado Denver
University of Denver
University of Utah
Utah State University
University of Wyoming

Technical Report Documentation Page

1. Report No.	2. Government Accession No.	3. Recipient's Catalog No.
MPC-609		

4. Title and Subtitle	5. Report Date
Durable Bridges Using Glass Fiber Reinforced Polymer and Hybrid Reinforced Concrete Columns	December 2023
	6. Performing Organization Code

7. Author(s)	8. Performing Organization Report No.
Dr. Chris P. Pantelides Duc Tran	MPC 23-511

9. Performing Organization Name and Address	10. Work Unit No. (TRAIS)
University of Utah Department of Civil and Environmental Engineering Meldrum Engineering Building Room 2115 Salt Lake City, UT 84112	11. Contract or Grant No.

12. Sponsoring Agency Name and Address	13. Type of Report and Period Covered
Mountain-Plains Consortium North Dakota State University PO Box 6050, Fargo, ND 58108	Final Report
	14. Sponsoring Agency Code

15. Supplementary Notes

Supported by a grant from the US DOT, University Transportation Centers Program

16. Abstract

Fiber reinforced polymer (FRP) composite materials have been studied and applied to reinforced concrete (RC) structures for strengthening or seismic retrofit for many years. This research is related to using FRP composites in new bridge structures. Capacity degradation in RC components of existing bridges occurs in harsh weather conditions when corroded steel reinforcement expands, which causes subsequent strength losses in concrete through the development of cracking and spalling. After significant earthquake events, RC structures undergo substantial residual displacement, which may cause instability and prevent the continued use of these structures. Accelerated bridge construction (ABC) has widespread construction applications with a new connection approach using semi-rigid corrugated steel ducts filled with ultra high-performance grout (UHPG). Based on these critical demands and developments, this report focuses on three main areas: (a) a hybrid longitudinal reinforcement system using conventional steel and glass fiber reinforced polymer (GFRP) longitudinal bars and GFRP spirals to resist corrosion and provide partial self-centering; (b) a post-tensioning system using all threaded, hot rolled, high-strength prestressing steel for self-centering capability; and (c) UHPG duct connections for ABC using one or both elements defined previously, i.e., hybrid reinforcement and post-tensioning. Four half-scale newly constructed columns with footing systems were tested under quasi-static cyclic loads simulating seismic effects. Experimental studies are conducted to facilitate the design and implementation of grouted duct connections with four types of columns: (1) all-steel longitudinal bars with GFRP spirals; (2) hybrid reinforcement in the form of longitudinal steel/GFRP bars with GFRP spirals; (3) all-steel longitudinal steel bars with GFRP spirals and post-tensioned high-strength steel rods, and (4) hybrid reinforcement in the form of longitudinal steel/GFRP bars with GFRP spirals and post-tensioned high-strength steel rods.

17. Key Word	18. Distribution Statement
bridge construction, carbon fibers, columns, fiber reinforced polymers, glass fibers, posttensioning, reinforced concrete bridges, tendons (materials)	Public distribution

19. Security Classif. (of this report)	20. Security Classif. (of this page)	21. No. of Pages	22. Price
Unclassified	Unclassified	57	n/a

Form DOT F 1700.7 (8-72) Reproduction of completed page authorized

Durable Bridges Using Glass Fiber Reinforced Polymer and Hybrid Reinforced Concrete Columns

Chris P. Pantelides
Professor

Duc Tran
Graduate Student

Department of Civil and Environmental Engineering
The University of Utah

December 2023

Acknowledgments

The authors acknowledge the financial support provided by the Mountain-Plains Consortium (MPC) under project MPC-609.

Disclaimer

The contents of this report reflect the views of the authors, who are responsible for the facts and the accuracy of the information presented. This document is disseminated under the sponsorship of the Department of Transportation, University Transportation Centers Program, in the interest of information exchange. The U.S. Government assumes no liability for the contents or use thereof.

ABSTRACT

Fiber reinforced polymer (FRP) composite materials have been studied and applied to reinforced concrete (RC) structures for strengthening or seismic retrofit for many years. This research is related to using FRP composites in new bridge structures. Capacity degradation in RC components of existing bridges occurs in harsh weather conditions when corroded steel reinforcement expands, which causes subsequent strength losses in concrete through the development of cracking and spalling. After significant earthquake events, RC structures undergo substantial residual displacement, which may cause instability and prevent the continued use of these structures. Accelerated bridge construction (ABC) has widespread construction applications with a new connection approach using semi-rigid corrugated steel ducts filled with ultra high-performance grout (UHPG). Based on these critical demands and developments, this report focuses on three main areas: (a) a hybrid longitudinal reinforcement system using conventional steel and glass fiber reinforced polymer (GFRP) longitudinal bars and GFRP spirals to resist corrosion and provide partial self-centering; (b) a post-tensioning system using all threaded, hot rolled, high-strength prestressing steel for self-centering capability; and (c) UHPG duct connections for ABC using one or both elements defined previously, i.e., hybrid reinforcement and post-tensioning. Four half-scale newly constructed columns with footing systems were tested under quasi-static cyclic loads simulating seismic effects. Experimental studies are conducted to facilitate the design and implementation of grouted duct connections with four types of columns: (1) all-steel longitudinal bars with GFRP spirals; (2) hybrid reinforcement in the form of longitudinal steel/GFRP bars with GFRP spirals; (3) all-steel longitudinal steel bars with GFRP spirals and post-tensioned high-strength steel rods, and (4) hybrid reinforcement in the form of longitudinal steel/GFRP bars with GFRP spirals and post-tensioned high-strength steel rods.

TABLE OF CONTENTS

LIST OF FIGURES

LIST OF TABLES

EXECUTIVE SUMMARY

During the service life of a bridge structure, the columns are exposed to harsh environmental conditions, which cause detrimental effects on structural strength. An earthquake has devastating consequences, including the collapse of bridge structures compromised due to corrosion-related concrete cracks and spalling. Post-earthquake residual displacements of bridge columns in bridges that did not collapse raise concerns about continued safety and use. This research proposes an ABC bridge system of corrosion-resisting columns with self-centering capability to reduce permanent displacement using ultra-high-performance grouted (UHPG) ducts.

Two specimens with precast concrete columns are investigated to assess the hybrid system's seismic performance using conventional steel and GFRP reinforcement. GFRP longitudinal bars and double GFRP spirals provide corrosion resistance and partial self-centering under cyclic loading. Two additional post-tensioned column specimens are investigated; post-tensioning is achieved using all-threaded prestressing bars to improve self-centering effectiveness using the exact reinforcement configuration as the first two specimens. All columns are connected to footings with corrugated galvanized ducts filled with lab-developed UHPG grout. The seismic performance of the four specimens was examined under quasi-static cyclic loads; all four specimens were found to perform in a satisfactory manner regarding strength and self-centering.

For the columns without post-tensioning, the lateral load capacity of the hybrid column was 9% less than that of the column with all-steel longitudinal bars. The hybrid column achieved a displacement ductility ratio of 4.0, while the column with all-steel longitudinal bars achieved a ductility ratio of 5.5. The elastic nature of the GFRP longitudinal bars provided substantial self-centering ability by reducing the residual displacement of the hybrid column, thus enhancing its seismic resilience.

Post-tensioned columns utilized high-strength all-threaded rods for post-tensioning; carbon fiber reinforced polymer (CFRP) wraps were externally used at the column bottom to protect the plastic hinge region. The seismic behavior of both precast concrete specimens was assessed through quasi-static cyclic tests; both columns exhibited satisfactory strength and deformability. The combination of post-tensioning bars with GFRP longitudinal bars was effective regarding self-centering ability. The residual displacement of the post-tensioned hybrid column was decreased by 46% compared with the post-tensioned all-steel reinforced column at 6.0% drift ratio. The elastic nature of the GFRP longitudinal bars provided substantial self-centering by reducing the residual displacements of the hybrid specimen, thereby enhancing seismic resilience.

LIST OF ACRONYMS

AASHTO	American Association of State Highway and Transportation Officials
ABC	Accelerated Bridge Construction
ACI	American Concrete Institute
ASTM	American Society of Testing and Materials
FHWA	Federal Highway Administration
PRESS	Precast Seismic Structural System
PT	Post-Tension
LVDT	Linear Variable Differential Transducer
UDOT	Utah Department of Transportation
UHPG	Ultra High-Performance Grout
NCHRP	National Cooperative Highway Research Program

1. INTRODUCTION

Accelerated bridge construction (ABC) utilizes prefabricated components to reduce the on-site work duration. This methodology enhances the safety of construction zones while reducing traffic delays and saving time and money. Since precast bridge elements are built off-site in strictly controlled conditions, product quality is ensured, and innovative materials and techniques are applicable for higher structural performance.

Various ABC connections, including but not limited to grouted ducts, mechanical rebar splices such as steel sleeves, pocket and socket connections, and stretch-length anchors, have been developed and implemented. Backed by experimental and analytical studies, connections between prefabricated components play a vital role in the structural performance of bridges designed to resist moderate and large earthquakes. An appropriate connection is capable of dissipating hysteretic energy while maintaining the structure's strength, stability, and integrity.

The seismic design of highway bridges allows inelastic/plastic performance of columns at selected locations during an earthquake. Columns are expected to undergo substantial inelastic deformation, resulting in permanent/residual displacement. Kawashima et al. (1998) observed that over 100 RC un-collapsed columns had a permanent residual drift ratio exceeding 1.75% after the 1995 Kobe earthquake. Residual displacement and drift ratio is a significant parameter of post-earthquake ability and functionality of bridges (Mackie and Stojadinovic 2004) and buildings (Bazzurro et al. 2004; Luco et al. 2004); this residual drift ratio is used to evaluate the serviceability and safety of use for structures following an earthquake. Hence, the self-centering capability of bridge columns emerges as an important technical issue for both new construction and retrofit of existing bridges.

Fiber reinforced polymer (FRP) composites have been studied and applied to RC structures that need strengthening or seismic retrofit. This practice, described in relevant documents published by the ACI 440 committee, involves structural rehabilitation utilizing externally bonded FRP laminates to alternative conventional techniques such as steel plates or sectional enlargement. Code guidelines initiated an increasing retrofit trend to meet the great demand for detrimental effects of steel reinforcement due to corrosion in concrete structures, particularly columns in bridges. As a result, the high cost of rehabilitation and disruption caused by bridge closures is reduced while the life span of bridge structures is extended. Experimental studies proved that externally wrapped carbon FRP layers can reduce corrosion effects. However, corrosion is not entirely prevented, which could lead to a loss in the ultimate axial capacity of columns (Bae and Belabri 2009). One approach is to replace some steel reinforcement in a column with glass FRP (GFRP) rebars and GFRP spirals to utilize the non-corrosive property of FRP.

This research project presents the effectiveness of an ABC duct connection filled with ultra high-performance grout (UHPG), which connects columns to footings; self-centering is achieved with GFRP reinforcement and unbonded post-tensioning systems. Combined with a proactive alternative of applying corrosion-free GFRP reinforcement in new bridge columns, the proposed columns in this study are economical and sustainable due to minimum maintenance or replacement.

1.1 Accelerated Bridge Construction (ABC) with Grouted Duct Connection

NCHRP Report 698 evaluated and summarized the performance of several ABC connections under moderate to high earthquake conditions. Grouted ducts, pocket connections, hybrid connections, integral connections, bar couplers, and emerging innovations such as elastomeric bearings and shape memory alloys were verified during the research. These connections were applied in practice or are being

investigated in studies for further real-world application. Criteria, including technology readiness and performance relative to cast-in-place construction and time-saving potential, were utilized to provide a ranking for connection types. This synthesis study promoted further essential research prioritized for each connection category to a complete understanding of their performance subject to seismic loading.

The grouted duct connection uses corrugated galvanized steel ducts embedded into one member with reinforcing dowels of another precast member inserted into the first component. The ducts are filled with high-strength grout to complete the joint. The forces from the longitudinal bars are transferred into the surrounding grout to the outside of the ducts. The load transfer mechanism of the grouted duct is in contrast with another popular connection type – bar coupler – where the load is transferred from one bar to another that is collinear with the first. Barton et al. (2022) investigated the combination of the grouted duct and grouted spliced sleeve connection in a manner that avoids mechanical couplers or sleeves in the plastic hinge region of the column or near the interface of column-to-footing or column-to-cap beam. The grouted duct technique is utilized for locations such as pile to pile cap, spread footing or pile cap to the column, column to cap beam, and splice between column or cap beam segments.

Matsumoto (2009b) and Pang et al. (2010) performed extensive tests under static loading and a few under cyclic loading for grouted ducts. Preliminary design guidelines have been formulated for seismic use (Restrepo et al. 2011; Matsumoto et al. 2001, 2008; PCI Design Handbook 2004) and are in the process of refinement. The connection type has been deployed in non-seismic regions and a few times in seismic regions (SR 520, Highways for LIFE).

The failure mechanism of reinforced concrete subject to aggressive environmental conditions is likely due to the corrosion of conventional steel reinforcement, starting from the stirrup and progressing to the steel longitudinal rebars. Several mitigation efforts have been introduced and applied, such as increasing concrete cover, replacing conventional steel with epoxy-coated, galvanized, or stainless steel, or adding admixtures to the concrete mix. These methods, however, do not resolve the root of the problem: steel is susceptible to corrosion, which can be prevented or limited but not eliminated. Fiber-reinforced polymer (FRP), a composite material system made of fibers and resin, emerges as an effective alternative reinforcement for concrete.

FRP rebars and stirrups provide significant merits over traditional steel, including corrosion resistance, high strength-to-weight ratio, transparency to magnetic fields, electrical and thermal non-conduction, and the ability to form any shape. These key benefits promote the application of FRP in concrete where structures exposed to potential corrosion require non-ferrous reinforcement or locations where machinery will “consume” reinforced concrete components, such as mining and tunneling. Based on structural design defined by the American Concrete Institute (ACI) and the American Association of State Highway and Transportation Officials (AASHTO), and bar properties defined by the American Society for Testing and Materials (ASTM) D7957, more than 600 installations in the U.S. and Canada have been erected with traditional procurement and construction methods.

1.2 FRP Reinforced Columns – Axial Performance

FRP mechanical properties involve higher tensile strength but lower modulus of elasticity than steel, anisotropic behavior with high strength in fiber direction and low shear strength and dowel action where resin dominates; moreover, FRP bars remain elastic up to failure, which implies FRP bars have no ductility. The FRP property of linear elastic stress-strain behavior exhibits some self-centering while the material returns to its original length, displaying no residual displacement after load removal. Stress-strain curves for various types of FRP and steel are presented in **Figure 1.1**. Hales et al. (2016) investigated high-strength slender concrete columns reinforced with GFRP rebars and spirals subjected to concentric and eccentric axial loads. GFRP longitudinal bars could promote more considerable deflections than steel

rebars due to their higher tensile strength and lower modulus of elasticity. In addition, they provide a self-centering effect, which is beneficial for transient-type loads such as earthquakes, once the load is no longer applied. On the other hand, steel longitudinal bars exhibit higher axial compression capacity and ductility than GFRP longitudinal bars due to their higher modulus of elasticity and yielding properties. As a result, combining steel and GFRP longitudinal bars with GFRP spirals provides the advantages of larger deflection capacity, ductility, self-centering effect, and better corrosion protection for reinforced concrete systems.

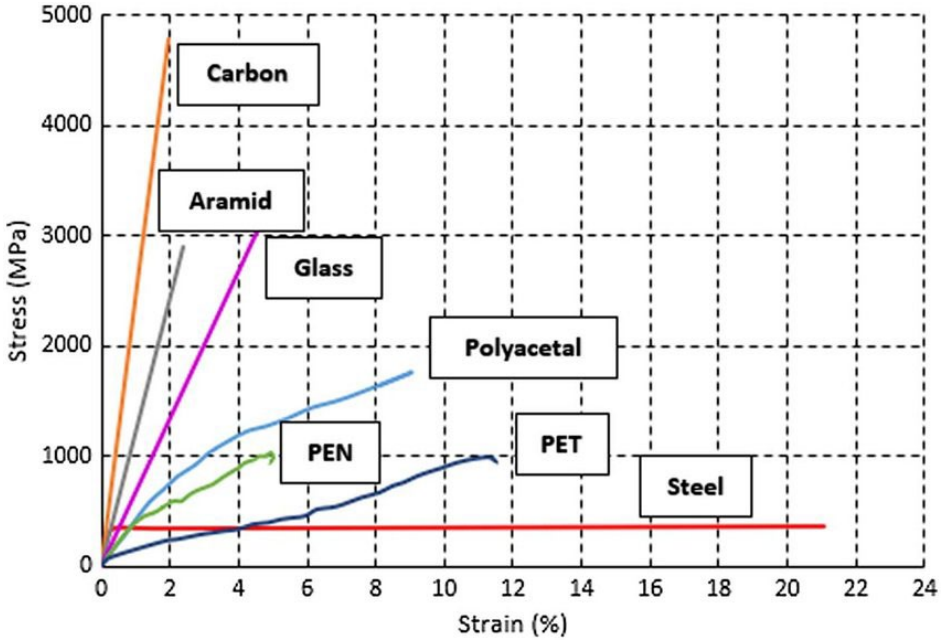

Figure 1.1 Stress-strain curves for several types of FRP and steel

Pantelides et al. (2013) investigated concrete confinement from glass FRP (GFRP) spirals in columns under axial load and determined whether GFRP spirals could reduce corrosion of longitudinal steel bars in hybrid columns. A total of 10 spirally reinforced concrete columns were evaluated, with six of the 254-mm diameter columns confined with a GFRP spiral and four confined with a steel spiral. Some columns employed steel longitudinal bars (hybrid columns), while others utilized GFRP vertical bars (all GFRP columns). The all-GFRP and hybrid columns achieved 84% and 87% of the axial load capacity compared with the all-steel control column. This indicates that hybrid columns must be reinforced with a larger GFRP spiral reinforcement ratio to achieve similar performance to all-steel columns. In comparison, all GFRP columns should be reinforced with a larger reinforcement ratio for both GFRP longitudinal bars and GFRP spirals; the authors observed that most corrosion occurred in the steel spiral, which raised concern about loss of confinement and brittle failure. For hybrid columns, some levels of corrosion were recorded through impressed current; however, no visible degradation in longitudinal steel existed in the columns. Corroded hybrid columns performed with a similar compression capacity relative to the all-steel corroded and control hybrid columns. Additionally, some of the hybrid and all-GFRP columns presented a more excellent ductility than the all-steel control columns.

In contrast, specimens reinforced with GFRP longitudinal bars and stainless-steel spiral achieved two to three times the maximum axial displacement of other series. In the case of columns exposed to a moderately corrosive environment after 60 days of continuous saturation in a saltwater solution with impressed current, specimens with 316L stainless clad longitudinal bars and GFRP spiral exhibited the highest axial compression capacity at 11.0% higher than the average. In comparison, columns reinforced

with all GFRP longitudinal and spiral reinforcement presented a 5.9% reduction in axial compression capacity.

Mohamed et al. (2014) evaluated the performance of concrete columns reinforced with longitudinal FRP bars confined with FRP spirals and hoops under concentric axial loads. The test findings showed behavioral similarities between the concrete columns reinforced with GFRP/CFRP bars and steel. The study also confirmed that the Canadian Standards Association S806-12 provisions on using GFRP and CFRP spirals or hoops provide sufficient restraint against buckling of the longitudinal FRP bars with good confinement of the concrete core in the post-peak stages.

Hadi et al. (2016) used GFRP rebars and GFRP spirals in concrete columns under different loading conditions. The test data indicated that the axial load and bending moment capacity of GFRP-reinforced columns were lower than those reinforced with steel. However, the ductility of the two column types was closely matched. It was also found that ignoring the compressive contribution of GFRP bars resulted in noticeable variances between experimental and analytical outcomes.

Maranan et al. (2016) investigated the performance of geopolymer-concrete circular columns reinforced with GFRP longitudinal bars and GFRP hoops under concentric axial loads. Short columns ($L/r = 8$) with different configurations of transverse reinforcement and slender columns ($L/r = 16$) transversely reinforced with hoops and spirals were evaluated. The test results showed that the contribution of GFRP bars to the overall capacity of the tested columns was 7.6% on average. Regarding slender columns confined with GFRP hoops and GFRP spirals, the column capacity was recorded as 66% and 82% of their short column counterparts. Spiral-confined columns also showed higher ductility and confinement efficiency than hoop-confined specimens.

Karim et al. (2016) examined the deformation behavior of circular concrete columns reinforced with GFRP bars and GFRP spirals. The test results showed that the strength and ductility of specimens increased as the pitch of GFRP spirals decreased; using CFRP wraps resulted in the same outcome. An analytical model for the axial deformation behavior of circular concrete columns reinforced with GFRP bars and spirals under axial loads was introduced and validated with test data.

Hadhood et al. (2017) examined the performance of concrete columns reinforced with GFRP bars and GFRP discrete hoops under combined axial load and bending moment. The test results revealed that confinement by GFRP hoops was sufficient to prevent buckling of GFRP longitudinal bars up to and beyond the peak load until failure occurred. Combining experimental and theoretical results, the minimum GFRP longitudinal ratio was estimated as 1.0% to avoid tension failure (GFRP bar fracture), provided that the mechanical properties complied with the limits of available codes and standards.

Elchalakani et al. (2017) studied the performance of GFRP-reinforced rectangular concrete columns under concentric and eccentric axial loading. The concrete columns reinforced with GFRP and thinner concrete cover exhibited more significant strain and deformation ductility than equivalent steel-reinforced concrete columns. It also verified that a smaller pitch of transverse reinforcement increased the load-carrying capacity and ductility of GFRP-reinforced columns.

Shankholkar et al. (2018) evaluated concrete confinement using GFRP spirals of small-scale cylindrical concrete specimens with a 254-mm diameter and 762-mm height under concentric axial compression. Wood dowels were used as longitudinal reinforcement to exclude the confinement contribution of longitudinal GFRP bars while maintaining a constant spiral pitch. The minimum confining pressure required to confine concrete and obtain compressive strength enhancement was 0.15 times the unconfined concrete strength. Concrete confinement improvement was higher for columns externally wrapped with FRP composite jackets than those internally reinforced with GFRP composite spirals.

Wright and Pantelides (2021) evaluated the axial compression performance of concrete columns reinforced with 316L stainless clad bars, 2304 duplex stainless bars and spiral, and GFRP bars and spiral after exposure to accelerated corrosion. For comparison, the hybrid columns reinforced with metallic and GFRP reinforcement and columns reinforced with GFRP longitudinal bars and GFRP spiral were also tested. One subset of columns was subjected to accelerated corrosion for 60 days. Columns reinforced with GFRP spiral achieved lower maximum displacements and presented sudden brittle failure compared with specimens reinforced with 2304 stainless steel spiral. All hybrid specimens provided more ductility than the all-GFRP specimens.

1.3 FRP/Hybrid Reinforced Columns – Seismic Performance

Zadeh et al. (2012) suggested that design guidelines did not cover FRP-reinforced concrete members subjected to flexural and axial loads simultaneously. Interaction diagrams were generated assuming GFRP longitudinal bars were effective in tension only; under compression, they could be replaced with the equivalent concrete area as if they were not present in the cross-section.

Liu et al. (2013) investigated the confinement effect of lateral FRP wraps on RC columns with minimal steel spirals. Test results indicated that higher axial load required greater confinement improvement from FRP wraps to reach a specific target ductility. The study also suggested that the confinement of large-pitch spirals in FRP-confined columns was unreliable and should be ignored in FRP-retrofit design.

Tavassoli et al. (2015) examined the seismic performance of circular columns fully reinforced with GFRP longitudinal bars and single spirals. These columns exhibited stable response regardless of the type of GFRP material used. Specimens under higher axial loads presented lower ductility and deformability levels while sustaining more damage. Conventional steel spirals provided effective confinement at the early stage, but their effectiveness was reduced once the steel yielded, allowing the concrete core to expand. In contrast, GFRP reinforcement offered increasing confinement with developing strain, delaying crushing the concrete core.

Ali et al. (2016) investigated eight columns with a 1,650-mm shear span and 350-mm square cross-section reinforced with GFRP bars under later quasi-static cyclic combined with axial loading; stirrup pitch, axial load level, and rebar type and ratio were studied. These GFRP-reinforced rectangular columns failed between a drift range of 8.5% and 12.5%, indicating that GFRP-reinforced concrete's deformability can replace the ductility of steel-reinforced concrete in dissipating earthquake energy.

Naqvi et al. (2017) examined the adequate splice length and varying axial load level effects in columns tested under simultaneous axial and quasi-static cyclic loads. The effect of steel fiber-reinforced concrete in inadequate splice-length columns was also investigated. To transfer the entire bond load along the splice length and maintain lateral strength capacity under higher axial loads and drift ratios, a splice length of 60 times the diameter of the longitudinal bar was reported to be adequate.

Kharal et al. (2018) investigated the seismic response of square GFRP spiral-confined concrete columns. The findings indicated that GFRP ties offered increasing confinement to the concrete core; rupture strain was much larger than steel yield strain, with the tie configuration influencing confinement effectiveness. The authors also made some suggestions for improvements, which are lacking in several aspects of current codes for GFRP ties.

Elshamandy et al. (2018) studied the ability of entirely GFRP-reinforced columns under reversed cyclic lateral load to reach the target drift required by various codes. Test results indicated that proper GFRP design details offered stable hysteresis performance with minimal strength degradation. GFRP-reinforced specimens confirmed that higher ultimate displacement could be reached than with steel-reinforced

columns. GFRP-reinforced columns reached a higher drift ranging from 50% to 180% higher than calculated per CSA S806 (2012), indicating the code is conservative.

Kharal et al. (2019) examined the seismic response of rectangular and circular columns confined by GFRP ties. Square columns confined by GFRP ties performed well under high axial load levels, and the compressive stress in GFRP longitudinal bars reached 60% of their tensile strength at column failure. In comparison, circular columns confined by GFRP spirals exhibited better ductility, strength, and total deformation performance than their rectangular counterparts. GFRP spiral strain in all columns was recorded to be much higher than 0.006, the maximum value prescribed in CSA S806 (CSA 2012).

Kharal et al. (2020a) studied the seismic response of large circular GFRP spiral-confined concrete columns. The test findings presented the confinement effect of the concrete core until rupture failure of the GFRP spirals, resulting in a strain level several times higher than the yield strain of mild steel. All the columns met the ductility requirements of the North American codes.

Kharal et al. (2020b) studied the seismic performance of square and circular GFRP/steel reinforced columns confined with GFRP rectilinear ties. Test data confirmed that GFRP confinement sufficiently improved the seismic capacity of the columns, regardless of the type of longitudinal bars. However, there were significant changes in column behavior with alternative longitudinal bars, as GFRP stirrups offered a greater flexural improvement on columns reinforced with GFRP longitudinal bars than those with steel bars.

Jia et al. (2021) proposed an alternative to precast segmental bridge column (PSBC), targeting higher durability performance in an aggressive coastal environment by incorporating longitudinal stainless steel and GFRP bars. The hybrid columns induced higher displacement ductility, less stiffness degradation, and smaller residual drift ratios than all stainless-steel specimens. In contrast, hybrid columns exhibited lower lateral loading capacity and hysteretic energy dissipation.

Abdallah et al. (2021a) studied the seismic response of GFRP-reinforced columns, precisely the effect of high-strength concrete (HSC) and varying spiral pitch and axial load. These well-confined circular columns offered seismic response with sufficient deformability. They surpassed the 2.5% and 4.0% drift ratio limits required by the National Building Code of Canada (NBC) and CSA S806-12 for ductile moment-resisting frames (MRFs), respectively.

Abdallah et al. (2021b) investigated the confinement properties of single-layer GFRP spirals/hoops in GFRP-reinforced concrete circular columns. Testing outcomes verified that the Canadian code for FRP-RC maximum spiral pitch of one-fourth the gross diameter of a column was safely conservative. On the other hand, it was found that a longer lap splice length than that specified by the Canadian Highway Bridge Design Code was required to exhibit equal performance to GFRP spirals.

Abdallah et al. (2022) also studied the effects of varying concrete strength, column aspect ratio, spiral pitch, and axial load levels on the seismic performance of GFRP-reinforced columns under lateral cyclic load. The increase of concrete strength from 35 to 80 MPa produced higher lateral capacity by 42% and 55% and lower drift capacity by 20% and 63% for a spiral pitch of 50 mm and 85 mm, respectively. High-strength concrete columns increased hysteretic energy dissipation by up to 71% compared with their normal-strength counterparts.

Arafa et al. (2022) studied columns with different ratios of longitudinal reinforcement and axial load to validate the finite element model (FEM) that considers the bond performance of GFRP bars and the nonlinear behavior of materials and geometries. Finite element analysis correctly simulated the performance of GFRP-reinforced concrete column tests. When failure was severe, the higher axial load presented localized damage in a small column length with significant permanent residual displacement. Recoverability and self-centering of columns were enhanced with higher longitudinal reinforcement.

Teng et al. (2015) developed a numerical model simulating the seismic response of reinforced concrete columns retrofitted with FRP confining jackets. Close agreement with test results of single- and double-curvature bending columns demonstrated success in predicting hysteresis response and energy dissipation.

Hamzeh et al. (2020) investigated the applicability of masonry shear walls reinforced with GFRP bars to achieve target strength and drift capacity. A numerical OpenSees macro-model was developed to predict the in-plane response of flexure-dominated reinforced masonry shear walls with boundary elements. The target design strength of GFRP-reinforced walls was achieved through a typical linear envelope curve with no strength degradation due to the natural elasticity of GFRP material, resulting in an increase in strength up to failure. These shear walls attained noticeably higher strength than steel, elastically performing up to near failure.

1.4 Rocking of Post-tensioning (PT) Columns

Billington and Yoon (2004), Ou et al. (2010), and Palermo et al. (2007) found that the hybrid rocking mechanism could be used in single-column bridge piers. With post-tensioning, large-scale single precast bridge columns can offer desired ductility and self-centering under high seismic load conditions (Ou et al. 2010 and Sideris et al. 2014). Palermo et al. (2007) investigated energy dissipation solutions using analytical studies and experimental quasi-cyclic tests on purely rocking monolithic hybrid columns. Further cyclic tests of post-tensioning precast concrete dual shell columns with supplemental energy dissipation devices were investigated by Guerrini et al. (2015) and proved effective self-centering up to an imposed 3% drift ratio. Experimental, analytical, and nonlinear analysis of hybrid bridge bents endorsed seismic resilience and significant reduction of residual displacement (Billington and Yoon 2004; Thapa et al. 2021; and Dangol et al. 2022).

2. EXPERIMENTAL PROGRAM

This chapter describes the design and construction of four experimental specimens and covers pull-out tests for the embedment length of GFRP bars in corrugated grouted ducts.

2.1 Embedded Length of GFRP #6 Bars in Grouted Ducts from Pull-Out Tests

Eight pull-out tests were performed in this study to investigate the minimum embedded length of M19 GFRP bars in 76-mm diameter UHPG ducts. The study by Brenes et al. (2006) on the grout-filled duct connection showed that the projected failure surface of a single bar in tension could be idealized as a square with sides equal to $15d_b$, as shown in **Figure 2.1**. In this study, specimen diameter (D) is designed as the sum of $15d_b$, spacing of ducts if any, and 102-mm tolerance for concrete cover and lifting bolts. For construction purposes, one diameter is considered for specimens: D = 406 mm. The height of samples (H) was assumed to equal the embedment length plus 127 mm. Since the embedment lengths are projected as $8d_b$, $10d_b$, $12d_b$, and $14d_b$, two heights of specimens are used: H = 305 mm for the embedment of $8d_b$ and $10d_b$, and H = 406 mm for the embedment of $12d_b$ and $14d_b$. **Figures 2.2 and 2.3** show the pull-out test setup.

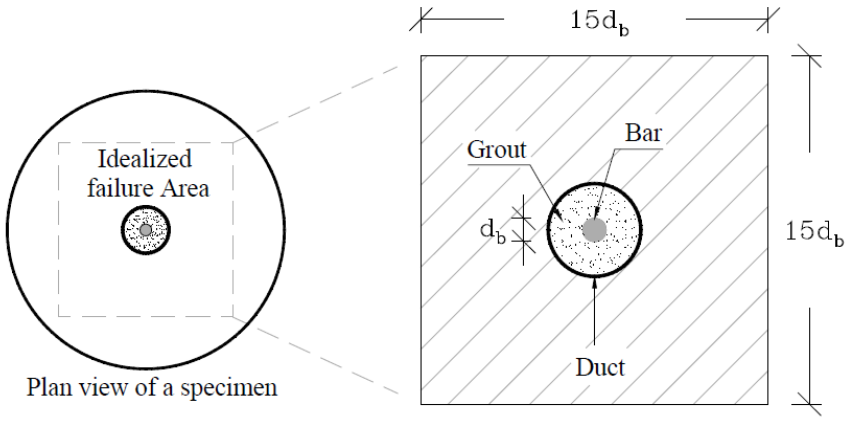

Figure 2.1 The pull-out projected failure surface

All specimens are lightly reinforced longitudinally with six M10 bars and transversely with M10 spirals at 51-mm pitch. The concrete cover was 25 mm in all specimens. The length of GFRP bars equals the sum of (L_{anchor}) plus 254 mm and ($L_{embedded}$).

Two specimens for each projected embedded length yield eight total tests. Several modes of failure are possible in grout-filled duct connections: (1) bar fracture, (2) bar pull-out caused by bond failure, (3) grout pull-out from the duct, and (4) duct pull-out by either failure of the bond between concrete surrounding the duct and the duct or conical failure of concrete.

This type of connection has two critical bond surfaces: the bar-grout interface and the grout-duct-concrete interface. These are carefully observed and examined during and after the tests.

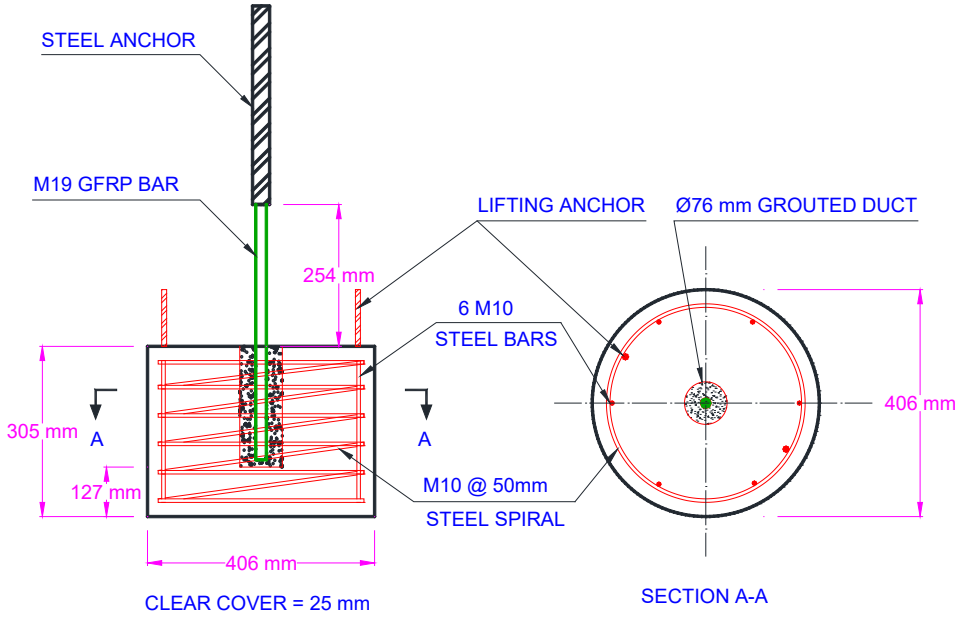

Figure 2.2 Configuration of $8d_b$ and $10d_b$ specimens

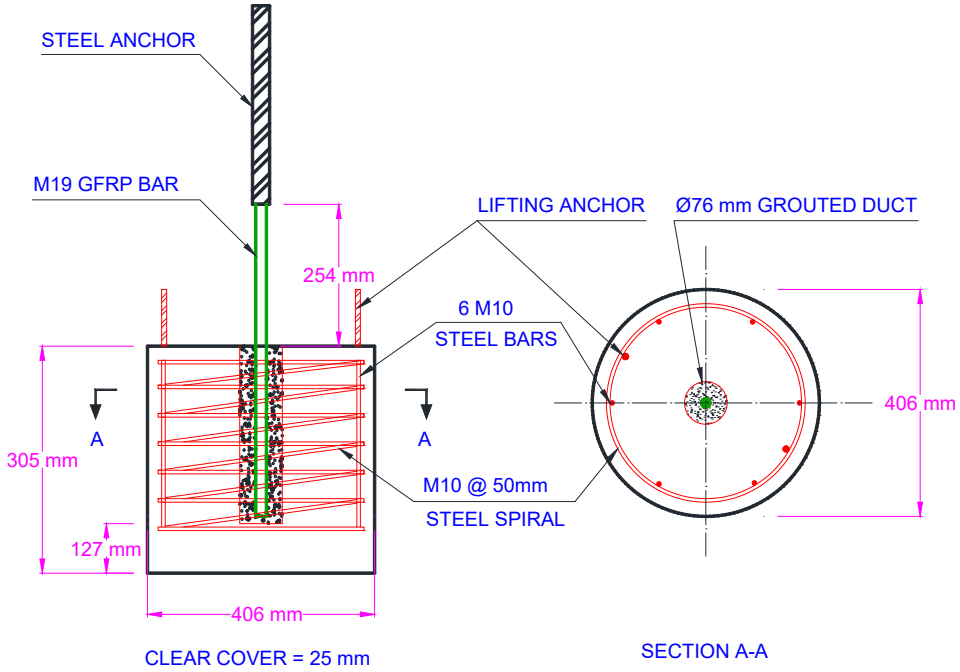

Figure 2.3 Configuration of $12d_b$ and $14d_b$ specimens

A new UHPG mixture is developed to reach the minimum compressive strength of 70 MPa. The coarse aggregates are excluded from the grout to accommodate the 51-mm pitch of column spirals, and silica fume is added to the batch to increase the compression capacity. MasterGlenium® 7500 Full-Range Water-Reducing Admixture is used to reduce the water/cement ratio for the high-strength performance of grout. Dosages of 15.6 liter/100 kg of cementitious materials are utilized. The admixture was divided into four batches with delayed addition to obtain optimum water reduction. This allows the grout's serviceability in column specimens' low-clearance reinforcement arrangements. **Table 2.1** displays the mix design of the UHPG.

Table 2.1. Ultra-high-performance grout (UHPG) mix design for 0.028 m^3 (1.0 ft^3)

Material	Specific Gravity	Weight		Volume	
		(kg)	(lbs)	(m^3)	(ft^3)
Sand	2.59	43.98	96.97	0.01680	0.60
Silica	2.2	2.66	5.87	0.00120	0.04
Cement	3.15	15.08	33.25	0.00474	0.17
Water	1	5.32	11.74	0.00527	0.19
Total Volume:				0.028	1.00

For data acquisition, one strain gauge is placed between the anchor and concrete top surface in the middle of the free length of 254 mm, as shown in **Figure 2.4**. The specimens are secured by anchoring the concrete block to the strong floor. The GFRP bar is stressed tension using a monotonic load through the fixed Aslan anchor until a failure mode is observed. **Figure 2.5** shows the construction of pull-out specimens.

Figure 2.4 Prepared bars with strain gauge installed

Two failure modes were recorded for the eight tests: bar pull-out and bar fracture. Bar pull-out failures were observed in both tests of $8d_b$ embedded length. Regarding $10d_b$, 12 d_b, and $14d_b$, the failure mode was bar fracture in tension, as shown in **Figure 2.6** and **Figure 2.7**.

Figure 2.5 Typical specimens before and after bar embedded

Figure 2.6 Failure modes: (a) bar fractured, (b) bar slipped out, or bar to grout bond failure

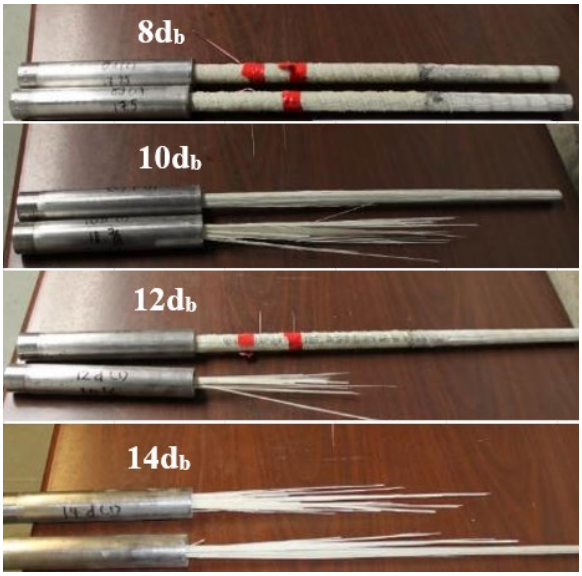

Figure 2.7 Bar failure after tests: $8d_b$ as bond failed (bar slipped out), $10d_b$, $12d_b$, & $14d_b$ as bar fractured

2.2 Experimental Design of Column Specimens

Four column specimens were constructed for testing; each included a column and a footing. These specimens were categorized into post-tensioning and non-post-tensioning groups. All columns contained two layers of longitudinal reinforcement, with an outer layer of longitudinal steel bars. This layer of steel reinforcement allows higher strain development while yielding steel properties that promote higher ductility and prevent abrupt failure. The inner layer was steel or GFRP longitudinal bars, which classified the columns as hybrid or all-steel systems. Double-layered GFRP spirals were adapted for all columns for enhanced corrosion resistance. Two all-threaded PT bars were provided for two of the specimens; in these two specimens, the PT bars were connected through embedded PVC pipes. Along with the elastic properties of GFRP reinforcement, PT bars contribute to the re-centering capability of the system. **Table 2.2** represents the test matrix associated with the experimental phase of the study.

Table 2.2 Test matrix

Test ID	Designation	Longitudinal Reinforcement	Post-Tensioning	CFRP Wrapping
1	HYB	6M19 Steel & 6M19 GFRP	None	None
2	STL	12M19 steel	None	None
3	PT-HYB	6M19 Steel & 6M19 GFRP	2M25 Threaded Bars	2 Layers
4	PT-STL	12M19 Steel	2M25 Threaded Bars	2 Layers

Based on typical prototype bridges in Utah, following the AASHTO LRFD Bridge Design Specifications (2012) and the AASHTO Guide Specifications for LRFD Seismic Bridge Design (2011), circular cages of longitudinal reinforcement and columns with an octagonal cross-section were adopted to facilitate the process of column precasting. The specimens in this study were half-scale models of typical prototype highway bridges in Utah.

2.2.1 Footing Configurations

The footings were designed for elastic performance and were identical for each column configuration. The dimensions of the rectangular foundation were 1,828-mm long, 914-mm wide, and 610-mm deep. Eight M25 steel bars equally spaced at 108 mm were used as top reinforcement. Two straight bar lap splices were used to accommodate the column core in the footing. Six M25 steel bars represented bottom longitudinal reinforcement, with four equally spaced at 108 mm in the middle and one at each outer edge. Both top and bottom steel bars are bent 90 degrees toward the center of the footing at the border to meet anchorage and development length requirements. Double hoops with 135-degree hooks spaced at 102 mm with M13 were used to enclose the longitudinal top and bottom reinforcement. The concrete cover was 51 mm in the footings. **Figure 2.8** shows details of the footing reinforcement.

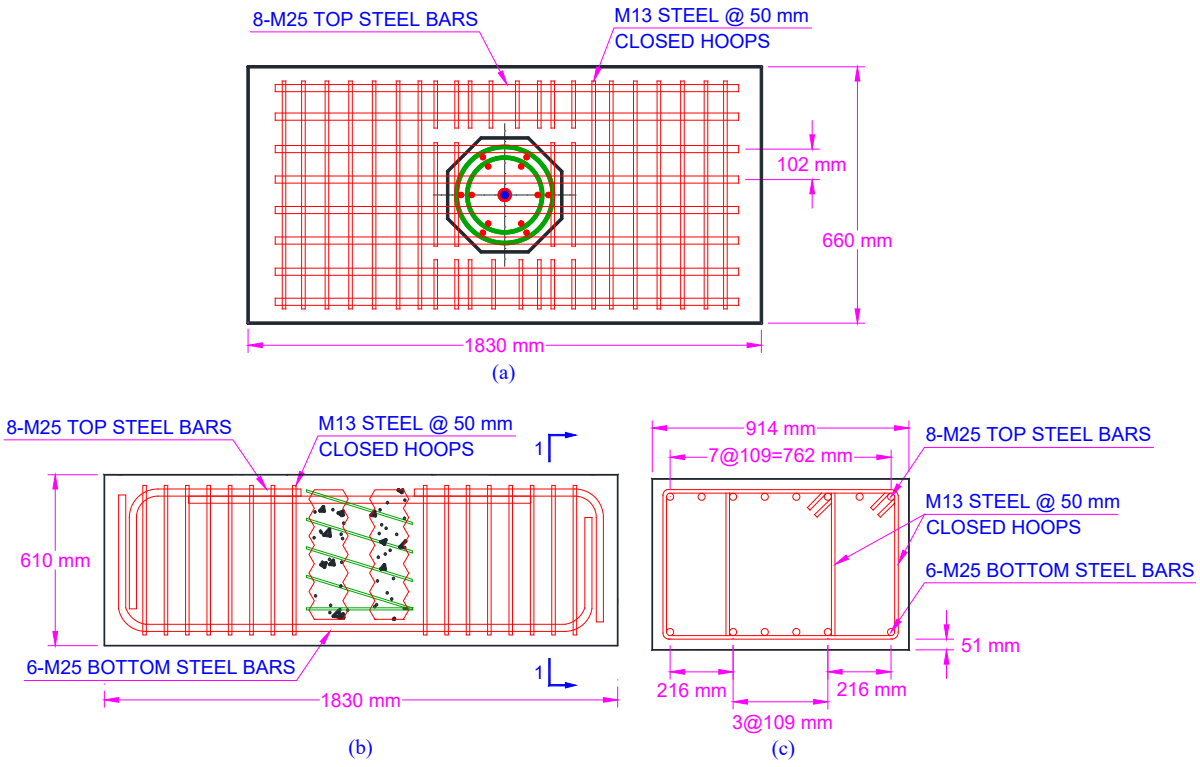

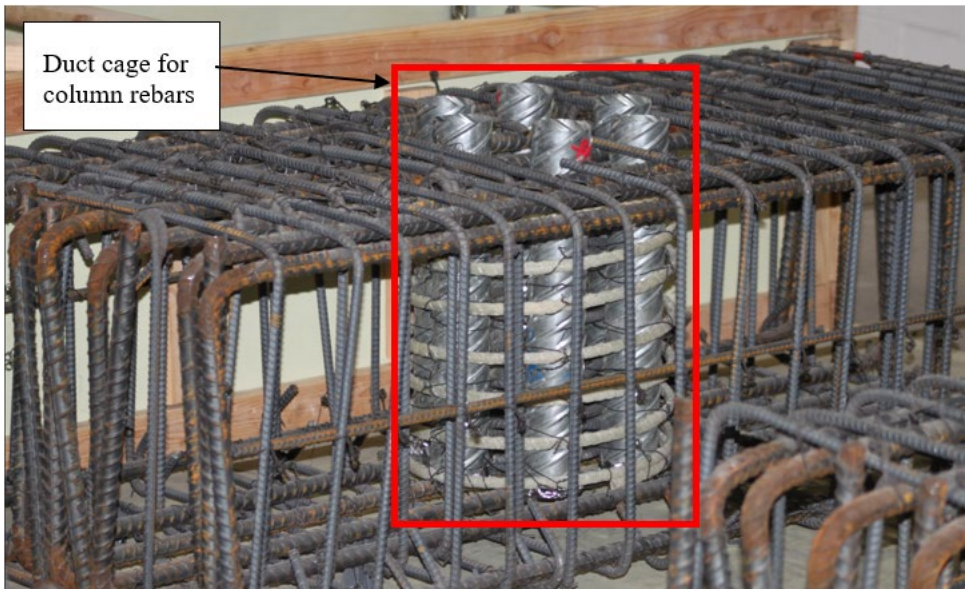

Figure 2.8 Footing configuration: (a) top view; (b) side view; (c) section 1-1; and (d) footing reinforcement cages

The column core cage was extended into the footing for precast compatibility. Six 76-mm diameter galvanized ducts were enclosed by M13 GFRP hoops spaced at 102 mm. Another layer of M13 steel rings was inside to secure these ducts' position. All ducts and post-tensioning pipes (for the PT group) were confirmed by a wood template shared by all footing and column components, as shown in **Figure 2.9**.

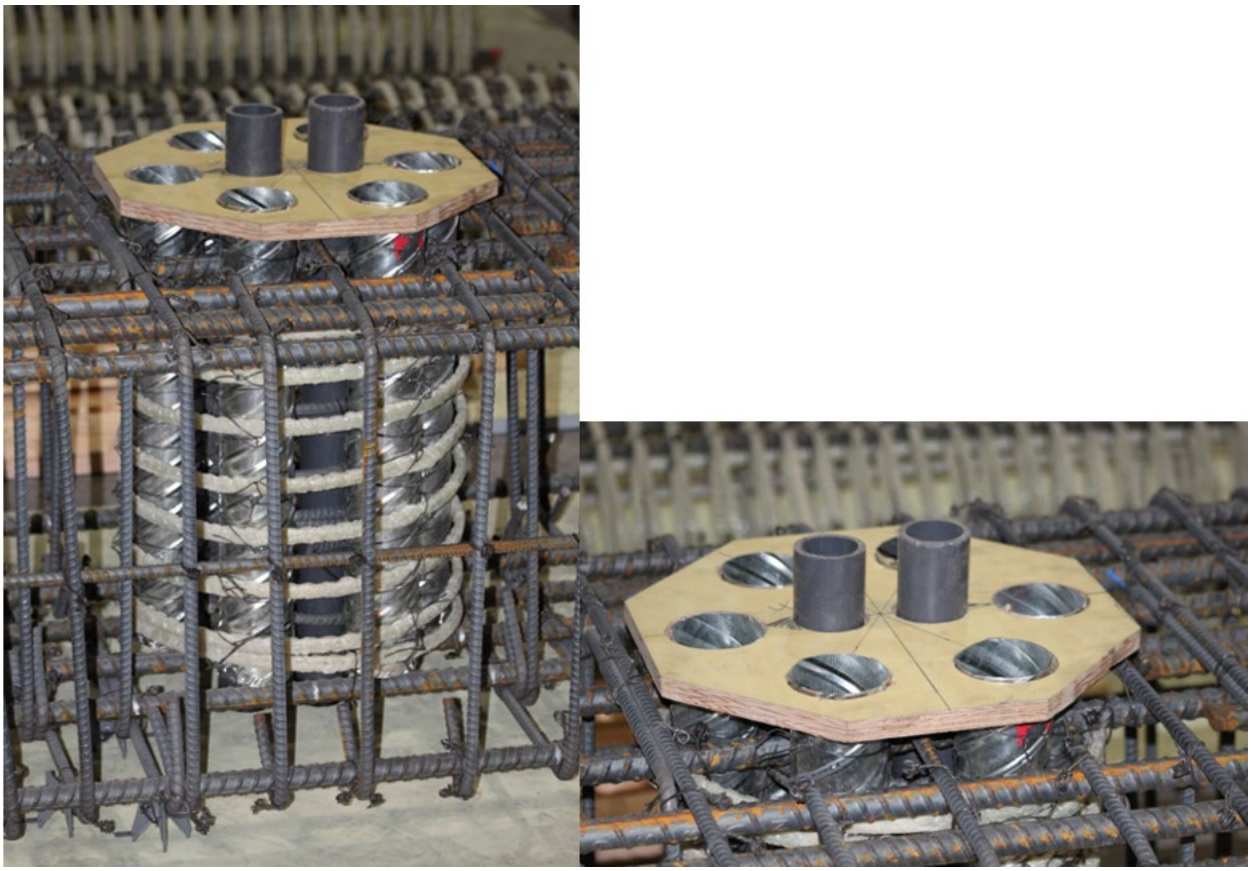

Figure 2.9 Column core in the footing and securing wood template

2.2.2 Column Configurations

Four columns were built for four specimens, as shown in **Figure 2.10 – Figure 2.13**. Each had a square column head of 406 mm in the top 406 mm. The lateral load from the actuator was applied at 203 mm from the top of this square segment. The column cross-section changed to an octagonal shape for ease of concrete precasting. The column was 2,489-mm long and reinforced with 12 M19 longitudinal bars arranged as two layers. Rebars were extended beyond the column's end to nest in galvanized ducts in the footings. Double layers of confining hoops were placed at 51-mm spacing with M13 GFRP. The concrete cover was 25 mm in the columns. The longitudinal reinforcement ratio of the column was 2.5%. Two 51-mm schedule 80 PVC pipes were used in each column to accommodate post-tensioning threaded bars after concrete casting. With a high-pressure rating and 5.5-mm thick, the 51-mm SCH 80 PVC pipe helped distribute strain evenly throughout the PT bars.

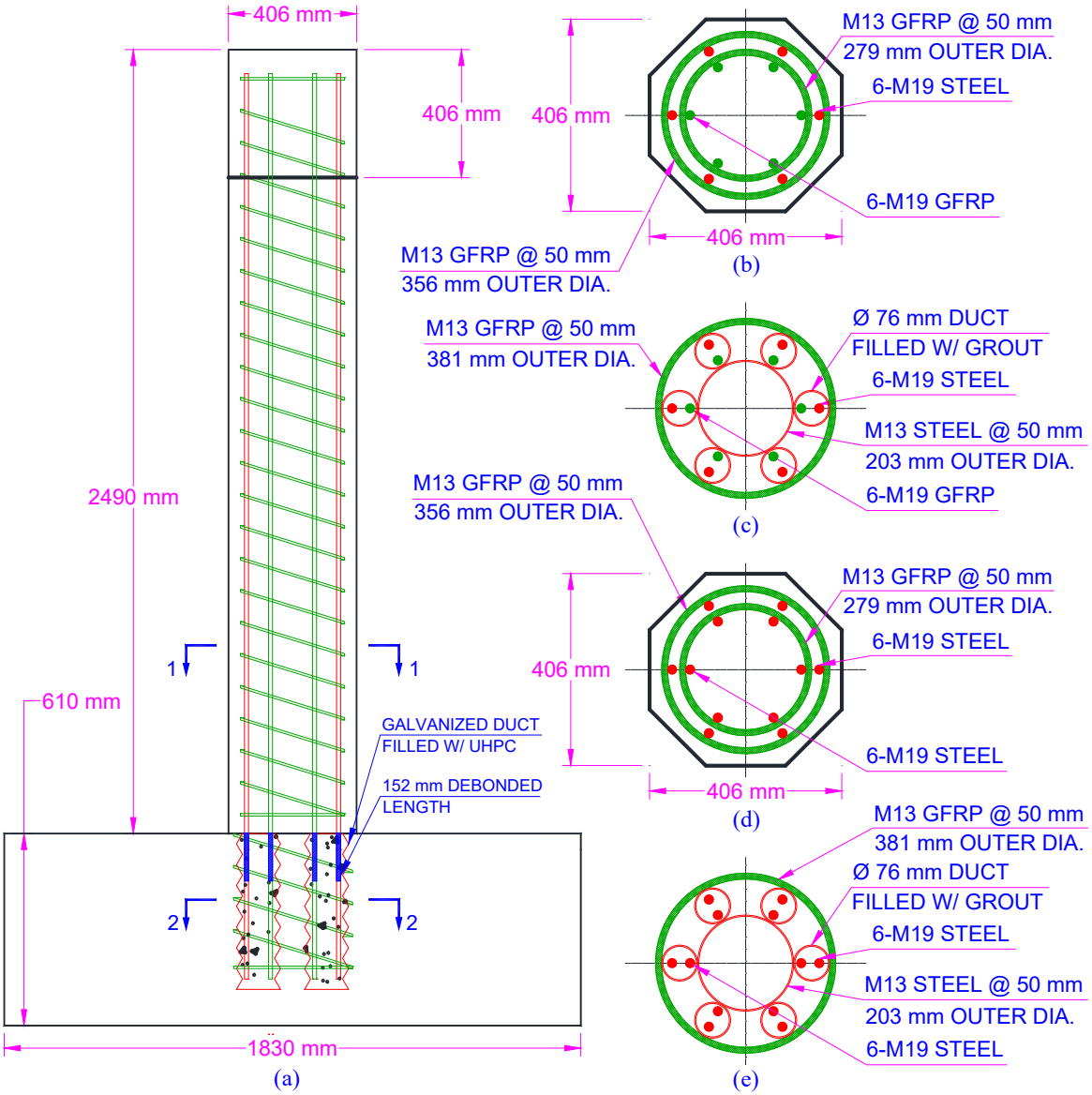

Figure 2.10 Non-PT column configuration: (a) side view; (b) section 1-1 HYB column;(c) section 2-2 HYB column; (d) section 1-1 STL column; (e) section 2-2 STL column

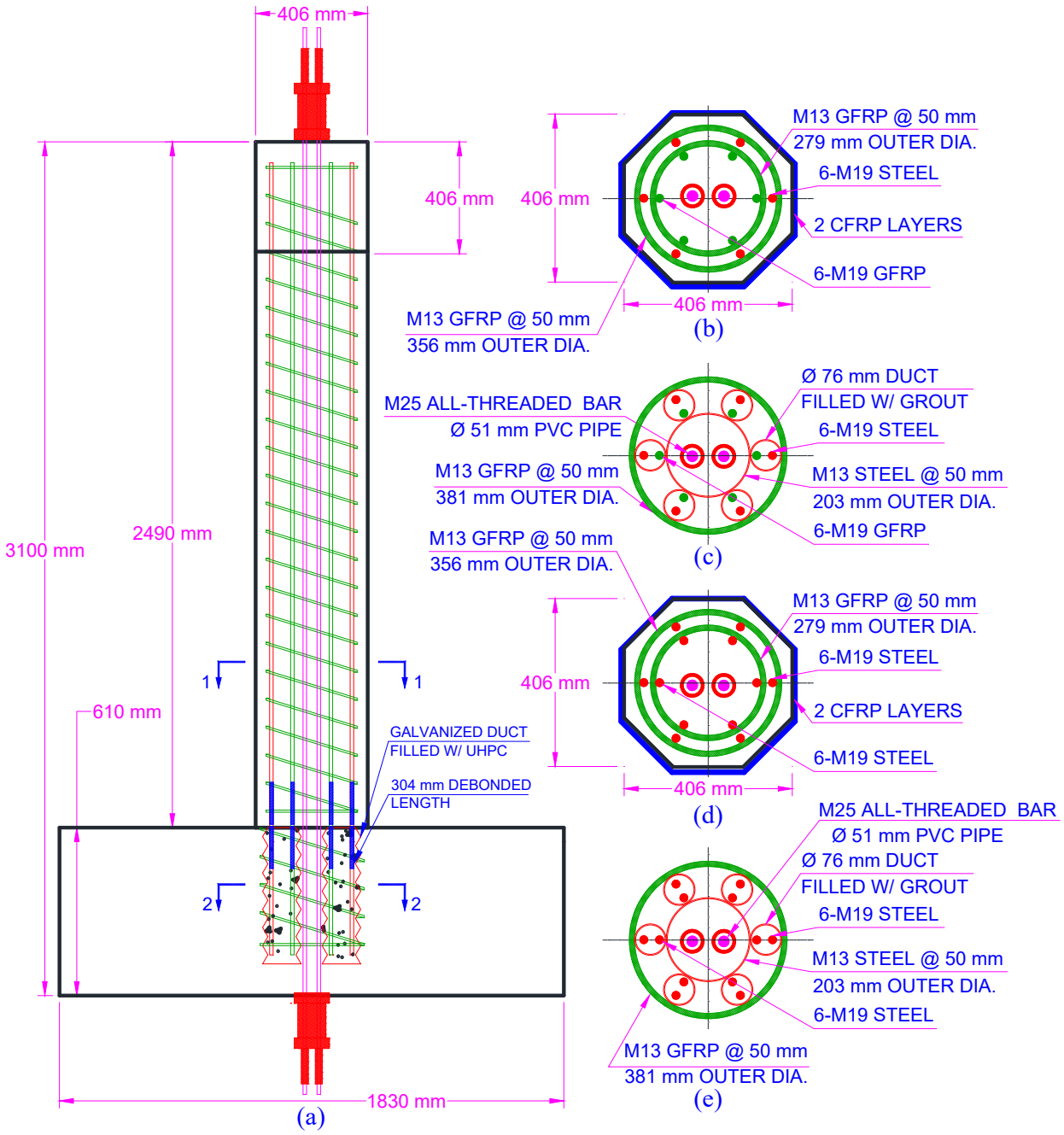

Figure 2.11 PT column configuration: (a) side view; (b) section 1-1 PT-HYB column; (c) section 2-2 PT-HYB column; (d) section 1-1 PT-STL column; (e) section 2-2PT- STL column

Figure 2.12 Column reinforcement cages

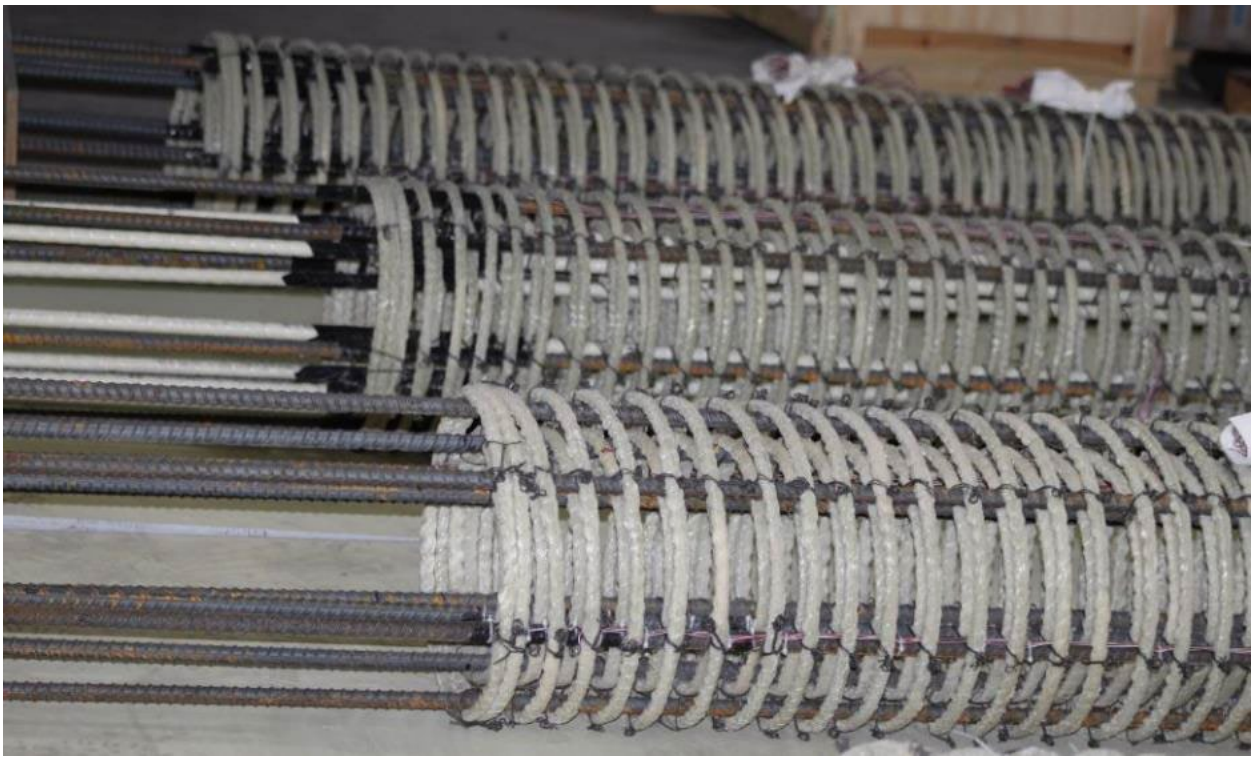

Figure 2.13 Column reinforcement details

2.2.3 Post-tensioning Rods

Two 1,034 MPa M25 threaded bars with a length of 3,302 mm were used for column post-tensioning. The bars are cold-stressed and stress-relieved in strict compliance with ASTM A722 and AASHTO M275 Highway Specifications. These PT bars are high in strength yet ductile for specified elongation and area reduction. The diameter of PT bars is 25 mm, with the minimum net area through threads being 549 mm^2. The minimum ultimate strength the manufacturer provides is 567 kN. The PT bars are appropriate for self-centering systems as they maintain an elastic performance of up to 80% of the ultimate strength or 454 kN. However, nonlinear performance can be found when surpassing 400 kN of tension, so the proper initial post-tensioning force is significant. The PT bar reinforcing ratio is 0.75%.

2.3 Material Properties

A total of 40 concrete cylinders of 102-mm diameter by 204-mm height was taken for self-consolidating concrete according to ASTM C31 (2019). The manufacturer's guaranteed compressive strength of concrete was 41 MPa. The 28-day compressive strength of concrete (f'_c) testing cylinders was above 45 MPa. Three standard concrete cylinders were tested on the specimen testing day. The average f'_c recorded ranged from 53 MPa to 61 MPa.

The yielding tensile strength of mild steel longitudinal reinforcement (f'_y) in the columns was 469 MPa. M19 GFRP longitudinal bars have a nominal area of 285 mm^2 with a guaranteed tensile strength of 690 MPa. This gives an ultimate tensile load of 197 kN. With the ultimate strain of 1.49%, GFRP bars have a tensile modulus of elasticity (E_f) of 46 GPa. M13 GFRP spirals have a guaranteed tensile strength of 780 MPa. The ultimate tensile load and strain are 95.9 kN and 1.64%, respectively. Three 965-mm long samples of 1034 MPa all-threaded bars were tested. The average ultimate stress recorded was 1,206 MPa.

2.4 Construction of Testing Specimens

All reinforcement cages were built in the structural laboratory of the Department of Civil and Environmental Engineering. Column bar cages were first constructed by passing six M19 inner longitudinal bars through M13 GFRP spiral hoops. These bars were then arranged and secured with a wooden template at each end. The bars were tied to the spiral at each hoop to the designated length to form a solid inner column rebar cage (double hoops at each cage's end for enhanced stability). Afterward, the wooden template at the top was removed, and the outer spirals were accommodated into the inner cage. The template was then brought back, and six M19 were passed through pre-drilled holes on the template and outer spiral hoops to achieve the second reinforcement layer. The tied connection between the bars and spirals was repeated to finish the reinforcement cage. Concrete spacers of 25 mm were tied along the cage to form the concrete cover when casting. For the PT specimens, two designated PVC pipes were passed through the cage using the template and steel rods to secure it in place.

The footing cages were started by building the joint core cage for the embedded longitudinal bars from the columns. Six 76-mm diameter corrugated galvanized ducts were secured vertically to M13 GFRP spiral hoops. A duplicated column wooden template with pre-drilled holes for ducts was used to match the column bars. Five M13 steel rings were installed inside to improve the stability of the cage. The footing reinforcement cages were constructed by tying four M25 bars to outer M13 spiral hoops at corners to form the overall shape of the cage. The first seven spiral hoops from each end were secured to longitudinal bars to accommodate the joint core. The joint core cage was then placed and tied into the footing cage, as shown in **Figure 2.9**. Lap splicing top bars and side spirals were installed to finish the cage. Concrete spacers of 51 mm were tied around the cage to form the concrete cover when casting.

The formwork of these specimens was constructed with 19-mm plywood, nails, and screws. Some plywood was cut at an angle to form the octagonal cross-section shape of the columns. The supporting structure for concrete casting was built with regular studs. All are demonstrated with site photos, as shown in **Figure 2.14 – 2.17**.

Figure 2.14 Column concrete casting formwork

Figure 2.15 Footing concrete casting formwork

Figure 2.16 Column concrete casting

Figure 2.17 Footing concrete casting

The precast columns and footings were assembled using the self-developed ultra-high-performance grout (UHPG) from the pull-out tests. As seen in **Figure 2.18**, 10-mm thick nuts were used as spacers to create the grout bed to accommodate concrete casting imperfections and excessive grout from the joint ducts. Wood templates were built to maintain the octagonal shape of the grout bed, as shown in **Figure 2.19**.

Figure 2.18 Nuts were used as spacers to create the grout bed

Figure 2.19 Specimen assembly with clamped wooden templates

2.5 Test Procedure

This section briefly describes the testing program with data instrumentations and acquisition. The instrumentation type, location, test setup, and loading protocol are presented.

Strain gauges were installed on the longitudinal and transverse reinforcement of the columns to monitor strain development during the test. The installation was mainly applied to the plastic hinge region of the column where the maximum stress was expected to occur. Other strain gauges were applied to extended bars inserted into the grouted ducts for strain development recording.

One string potentiometer was used to record column lateral displacement during the test; it was attached to the column head at the same elevation as the actuator centerline axis. Column lateral displacement was verified with the actuator's temposonic reading.

Linear variable differential transformers (LVDTs) were set up to monitor the curvature distribution along the column's bottom end. These instruments were used to verify the vertical and horizontal movement of the test specimens, characterizing bond-slip rotation and base rotation of the joint connection. Ten LVDTs were installed over approximately 635 mm of the column end to monitor each section's relative vertical displacement and curvature. Two LVDTs connected the column and footing and provided data for column base rotation and, subsequently, bond-slip calculation.

The specimens were fixed to the rigid floor with eight high-strength threaded bars passing through embedded PVC pipes in the footing.

Axial load was applied to the column using a cylindrical 2,224 kN hydraulic actuator sitting on the column top with a 1,219-mm long stiffened W14x90 spreader beam and two 38-mm diameter 1,034 MPa all-threaded rods, as shown in **Figure 2.23**. The hydraulic actuator extends out to create tension in the all-threaded rods, which results in a compression reaction onto the column. An initial 6% axial column capacity load was applied to simulate the gravity load always present on a bridge column. The values of axial loads ranged from 503 kN to 574 kN due to varying concrete compressive strength when the columns were tested. These values corresponded to 6% of the axial capacity of the columns and remained constant during the test. A custom steel box was built for PT columns to accommodate the PT bars and transfer the axial load to the columns, as shown in **Figure 2.20 – 2.22**. Axial loads were adjusted to reach 6% of axial capacity during the post-tensioning procedure.

Figure 2.20 Custom steel box for axial load transfer in post-tensioning columns

Figure 2.21 PT bars were installed before setting the axial load mechanism

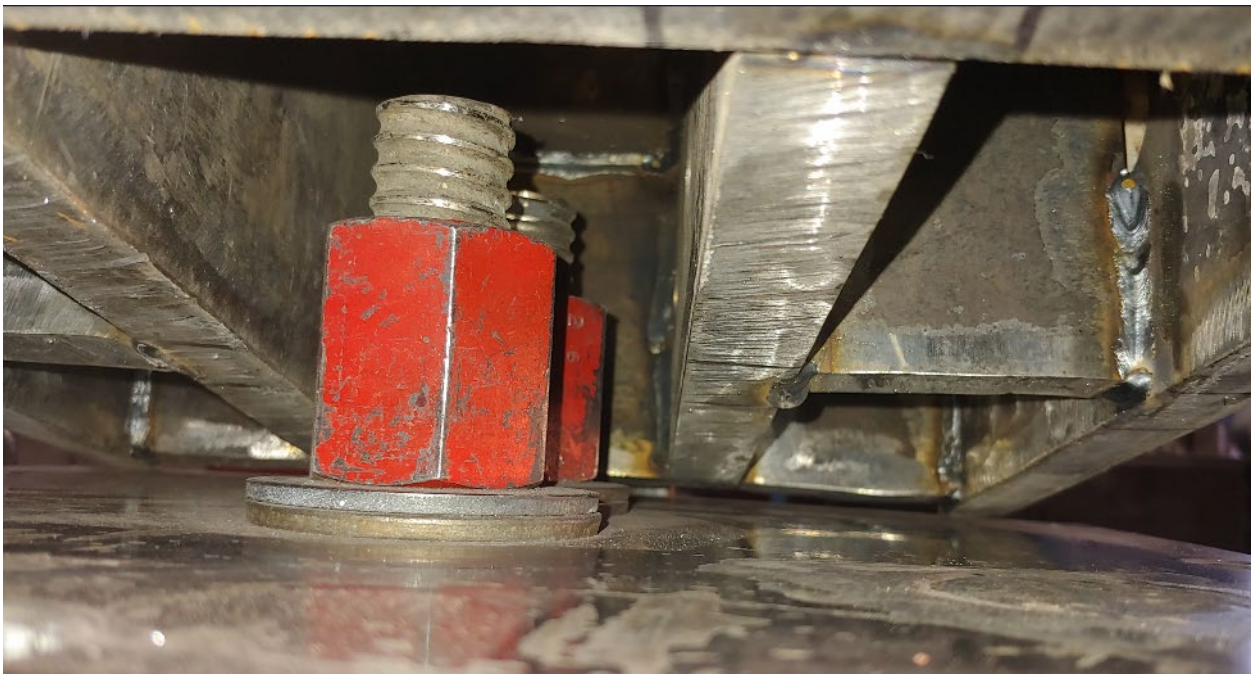

Figure 2.22 PT bars were nested inside the custom steel box

Figure 2.23 The complete top setup of the axial load for PT columns

A load cell rated at 752 kN was installed on each PT threaded bar to record the PT force during the test. The load cells were applied at the bottom of the footing to accommodate the axial mechanism on top of specimens, as shown in **Figure 2.24**.

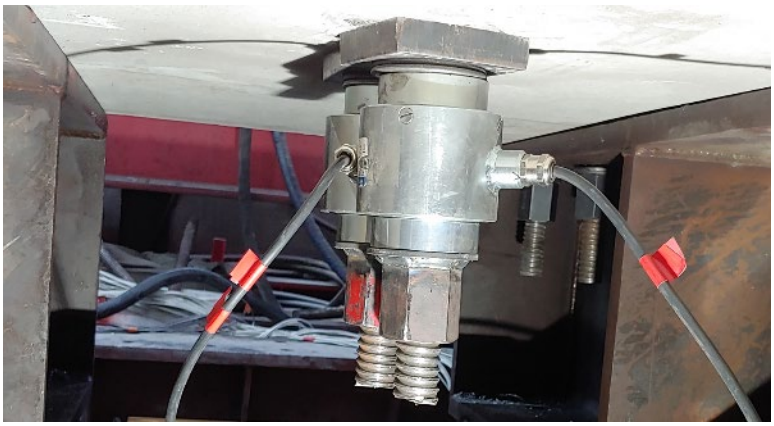

Figure 2.24 Load cell setup

A quasi-static displacement-controlled loading protocol was applied to the column at 2,210 mm above the footing, as shown in **Figure 2.25**. Two sine-wave cycles were employed at each increasing amplitude drift ratio. An 801 kN servo-controlled actuator, with an overall 533-mm stroke, was used to apply the simulated cyclic load on the specimens.

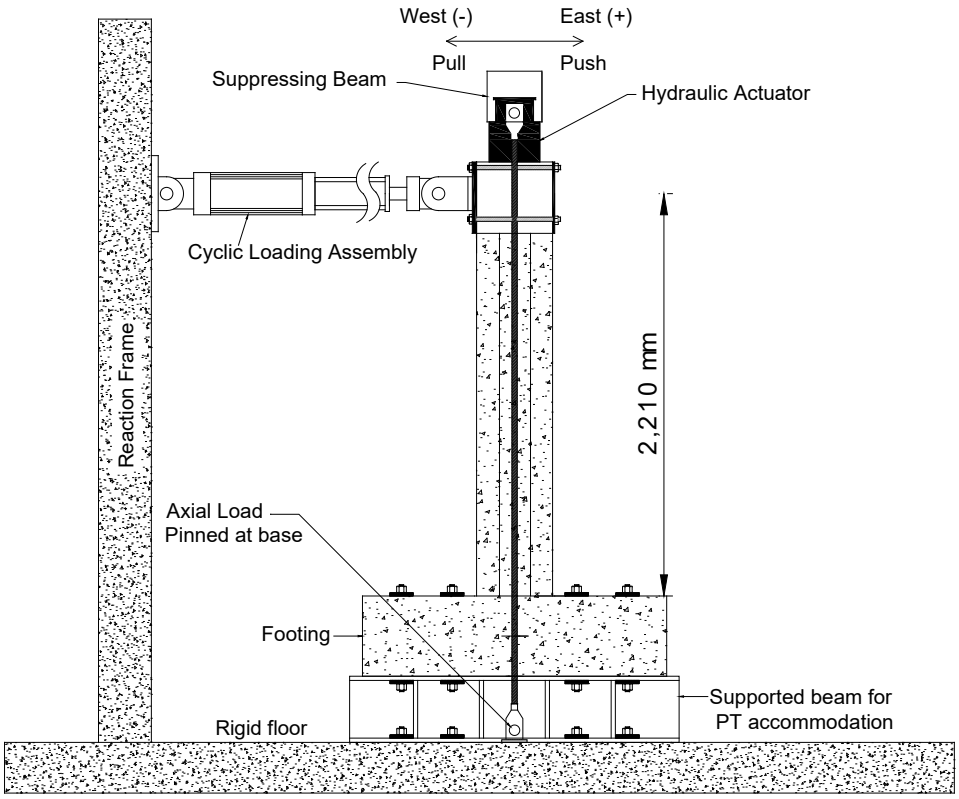

Figure 2.25 Schematic test setup

The drift ratio is the lateral displacement divided by the influential (unbraced) column height, taken here as 2,210 mm. Two complete sine-wave cycles were introduced for each drift ratio at 0.5%, 1.0%, 1.5%, 2.0%, 3.0%, 4.0%, 5.0%, 6.0%, 7.0%, 8.0%, 9.0%, 10%, and 11%, as shown in **Figure 2.26**. The displacement rate was 30.5 mm per minute for drift ratios up to 3.0% and 102 mm per minute for drift ratios from 4.0% and higher. The testing procedure stopped automatically after finishing the 12% drift cycles after reaching the actuator maximum stroke limit, or the specimen's load capacity dropped more than 20%. **Figure 2.27** shows the experimental setup.

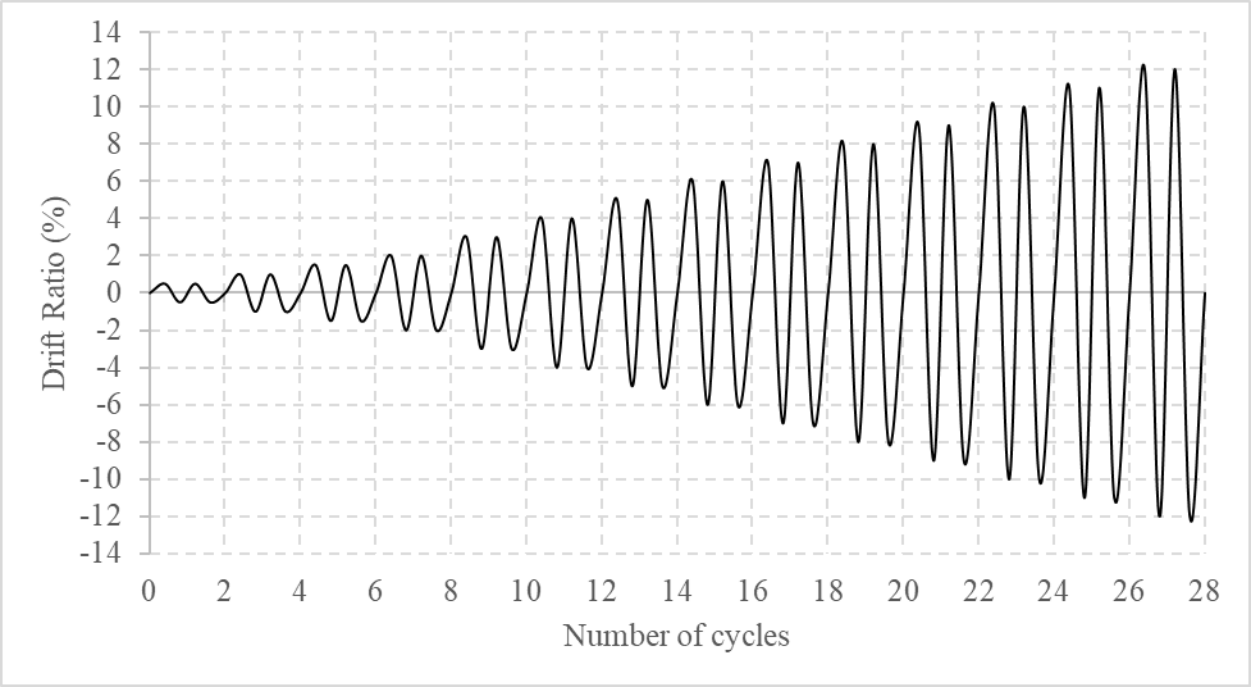

Figure 2.26 Loading protocol

Figure 2.27 Experimental configuration for column test

3. TEST RESULTS

3.1 Non-PT Specimens

3.1.1 Hybrid column (HYB)

Figure 3.1(a) illustrates the hysteresis behavior of the HYB column. Hairline cracks initially appeared in the grout at a drift ratio of 1.5%, and they gradually extended around the column. When the drift ratio reached 2.0%, the column began to separate from the grout bed. Hairline cracks emerged vertically and horizontally at a 3.0% drift ratio in a 150-mm high zone. These cracks continued to propagate, and by the time the drift ratio reached 4.0%, they had expanded into 250-mm high regions, with some cracks widening to 0.4 mm, accompanied by concrete spalling in the grout bed. On the bottom east side, a 75-mm concrete section spalled off. At a 5.0% drift ratio, a 200x250-mm concrete section fell off, exposing the outer layer of GFRP spirals on the west side, while the east side experienced a 400x200-mm concrete spall with no reinforcement exposure. The spalling continued to progress at the 6.0% drift ratio, reaching a height of 250 mm and exposing the outer layer of the GFRP spirals on both the east and west sides. At drift ratios of 7.0% and 8.0%, a 0.3-mm wide crack extended to heights of 400 mm and 600 mm, respectively. When the drift ratio reached 9.0%, a GFRP longitudinal bar on the west side of the inner layer of longitudinal reinforcement fractured in compression.

At a 10.0% drift ratio, the west extreme steel bar and one turn of the GFRP outer spiral fractured. A northwest steel bar buckled, a northeast steel bar fractured, and one more turn of the GFRP outer spiral fractured at the west extreme side. It is important to note that the fracture of the outer GFRP spirals was a localized failure due to the buckling of the vertical steel bars, and no fractures were observed in any of the inner GFRP spirals. **Figure 3.1(a)** indicates that the lateral force in the column gradually increased up to a 9.0% drift ratio, reaching a lateral force capacity of 120 kN, corresponding to 197 mm of lateral displacement at the 9.0% drift ratio. This performance can be attributed to the contribution of the longitudinal GFRP bars, as they maintain linear elastic behavior until they fracture. Extensive spalling at a 6.0% drift ratio is depicted in **Figure 3.2(a)**, while **Figure 3.2(b)** shows GFRP longitudinal bar compressive fracture and steel bar tensile fracture at an 11.0% drift ratio.

3.1.2 All-steel longitudinal column (STL)

At the 2.0% drift ratio, the appearance of hairline cracks and the emergence of separation between the column and the grout bed marked the beginning of structural issues. These cracks extended to a 200-mm height, and minor concrete spalling was observed at the 3.0% drift ratio. By the time the drift ratio reached 4.0%, a section of concrete measuring 200x150 mm had spalled off, and the cracks had widened to 0.35 mm, reaching a height of 250 mm. Concrete spalling expanded to 400x400 mm, exposing the GFRP outer spiral on both sides during the 5.0% drift ratio, which occurred earlier than in the hybrid column.

At the 6.0% drift ratio, horizontal concrete cover spalling was noted, with the primary concrete failure occurring 300 mm from the column bottom. Concrete damage and cracks continued until the 11.0% drift ratio when the outer steel bar and two turns of the outer GFRP spiral on the west side fractured. Additionally, the outer steel bar on the extreme east side also fractured. Notably, the inner GFRP spiral remained intact, and the inner layer of longitudinal steel reinforcing bars did not experience any fractures. **Figure 3.1(b)** illustrates the performance of the all-steel longitudinal column, which exhibited high stiffness until the 3.0% drift ratio when it reached a plateau. The column demonstrated a lateral load capacity of 130 kN, equivalent to a displacement of 123 mm during the 6.0% drift ratio. Concrete spalling

is visible in **Figure 3.2(c)** at the 6.0% drift ratio, while **Figure 3.2(d)** shows longitudinal steel bar fractures and outer GFRP spiral fractures at the 11.0% drift ratio.

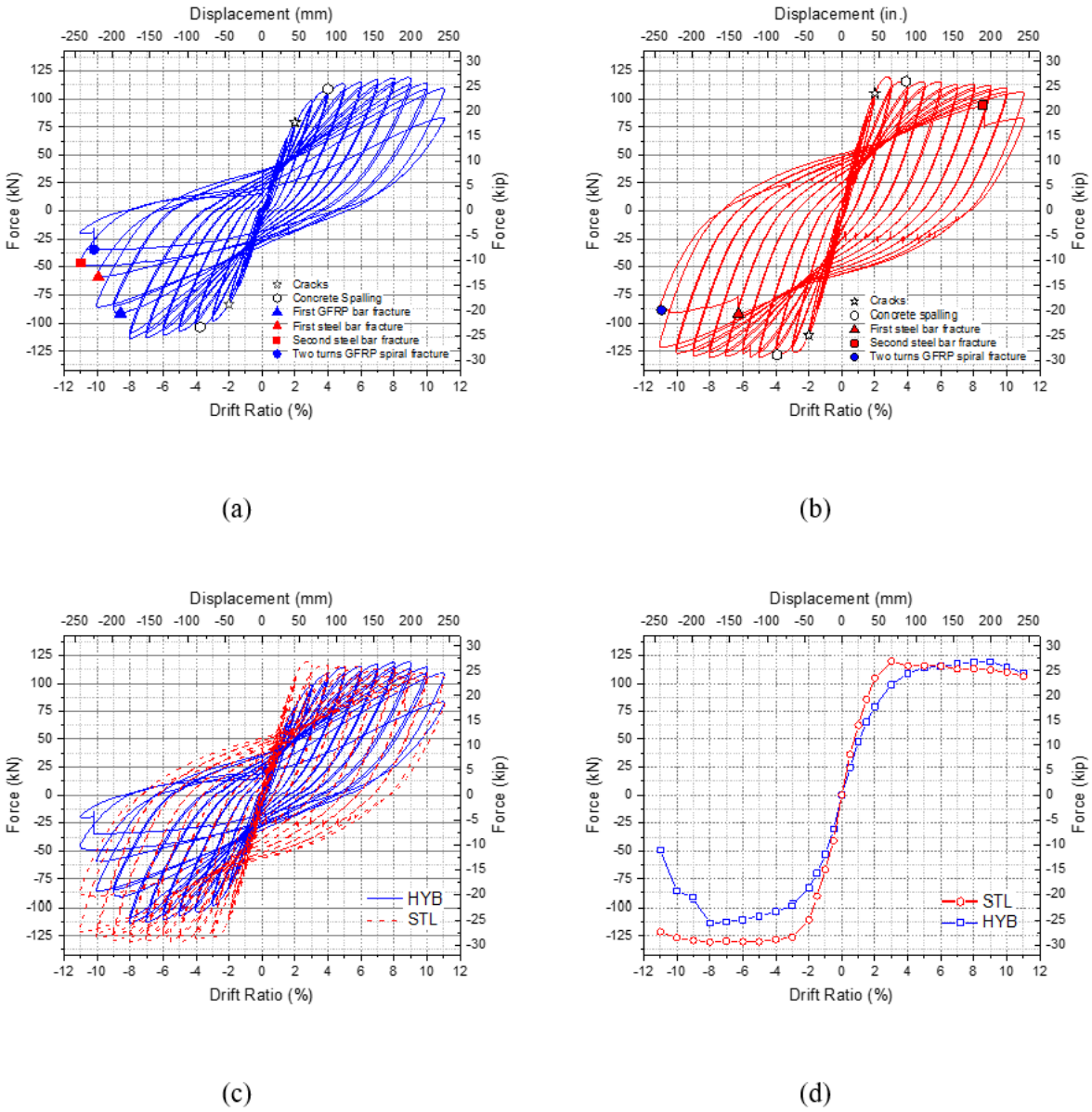

Figure 3.1 Non-PT column hysteresis: (a) HYB hysteresis; (b) STL hysteresis; (c) hysteretic comparison; and (d) hysteretic envelope

(a) (b)

(c) (d)

Figure 3.2 Non-PT column damage: (a) HYB at 6.0% drift ratio; (b) HYB at 11.0% drift ratio; (c) STL at 6.0% drift ratio; and (d) STL at 11.0% drift ratio

3.2 PT Specimens

3.2.1 PT Hybrid column (PT-HYB)

Figure 3.3(a) reveals an increase in lateral force within the column as the drift ratio advances, with a lateral force of 193 kN reached, corresponding to a 221-mm lateral displacement during the 10.0% drift ratio. The observed performance can be attributed to longitudinal GFRP bars, which remained linear elastic until fracture. **Figures 3.4(a) and 3.4(b)** illustrate the condition of the column at the end of the test at the 12.0% drift ratio. Notably, the damage sequence started with hairline cracks forming in the grout during the initial 1.5% drift ratio cycle and progressing around the column. Separation of the column from the grout bed became evident at the 3.0% drift ratio. By the time the drift ratio reached 5.0%, the edge of the CFRP wrap began to unravel, and hairline cracks emerged in the concrete above the top of the CFRP wrap. At the 6.0% drift ratio, cracks developed in the CFRP wrap on both sides, situated at a height of 508 mm above the footing. Horizontal cracks, measuring 0.2 mm and 0.3 mm in width, were observed at the interface of the CFRP wrap and concrete on the east and west sides, respectively. The width of the concrete cracks increased to 0.8 mm, while the horizontal cracks in the CFRP wrap expanded to a width of 0.6 mm during the 7.0% drift ratio. New horizontal concrete cracks emerged 915 mm above the footing, accompanied by minor concrete spalling. At the 8.0% drift ratio, the concrete cracks widened to 0.8 mm, with additional spalling. New concrete cracks were also recorded at a higher elevation, up to 1,200 mm above the footing. Significant concrete spalling occurred during the 9.0% drift ratio, involving concrete pieces measuring 250x150 mm on the west side and 250x100 mm on the east side. These incidents were accompanied by progressive horizontal cracks extending up to 1,400 mm above the footing.

At the 10.0% drift ratio, the concrete damage continued to expand, with additional horizontal cracks in the CFRP wrap on the east side. The specimen experienced a CFRP wrap fracture of a 50-mm-wide strip at the bottom of the column on the west side, as depicted in **Figure 3.4(a)**. Further concrete cracks and spalling developed during the 11.0% drift ratio, ultimately leading to concrete crushing at the base of the column, precisely at the location of the fractured CFRP wrap. At the 11.0% drift ratio, one mild steel bar from the outside layer of longitudinal reinforcement fractured on the west side, as revealed in **Figure 3.4(b)**. Notably, there were no observed fractures of GFRP bars or GFRP spirals.

3.2.2 PT All-steel longitudinal column (PT-STL)

Figure 3.3(b) depicts the performance of the all-steel longitudinal column, which exhibited a high stiffness until the 6.0% drift ratio and then reached a plateau for higher drift levels. This column achieved a lateral load capacity of 184 kN, corresponding to a 155-mm displacement during the 7.0% drift ratio. The state of damage at the end of the test at the 12.0% drift ratio is illustrated in **Figures 3.4(c) and 3.4(d)**. The sequence of damage initiation began with hairline cracks in the bed grout at both extreme sides of the column at the 1.5% drift ratio. By the 3.0% drift ratio, the separation of the column from the grout bed had become evident. Hairline cracks also emerged at 510 mm above the top of the CFRP wrap. The first crack in the CFRP wrap appeared on the east side, located 410 mm above the footing. At the 4.0% drift ratio, concrete cracks developed at a height of 1,000 mm above the CFRP wrap, and a new crack formed on the west side of the CFRP wrap at a height of 460 mm above the footing. These concrete cracks expanded to a width of 0.25 mm and were accompanied by horizontal cracks in the CFRP wrap at the 5.0% drift ratio. As the drift ratio increased, more CFRP cracks emerged, ultimately leading to concrete crushing at the base of the column during the 8.0% drift ratio. At the 9.0% drift ratio, a 50-mm-wide strip of carbon wrap fractured on the west side at the bottom of the column, as depicted in **Figure 3.4(c).**

During the 10.0% drift ratio, concrete crushing at the base of the column was observed after the fracture of a strip of CFRP wrap. Subsequently, at the 11.0% drift ratio, the first steel bar fractured on the west side; at the 12.0% drift ratio, a second steel bar fractured on the east side, as seen in **Figure 3.4(d)**. Both fractures occurred on the outer layer of longitudinal mild steel bars. Notably, there were no fractures of GFRP spirals.

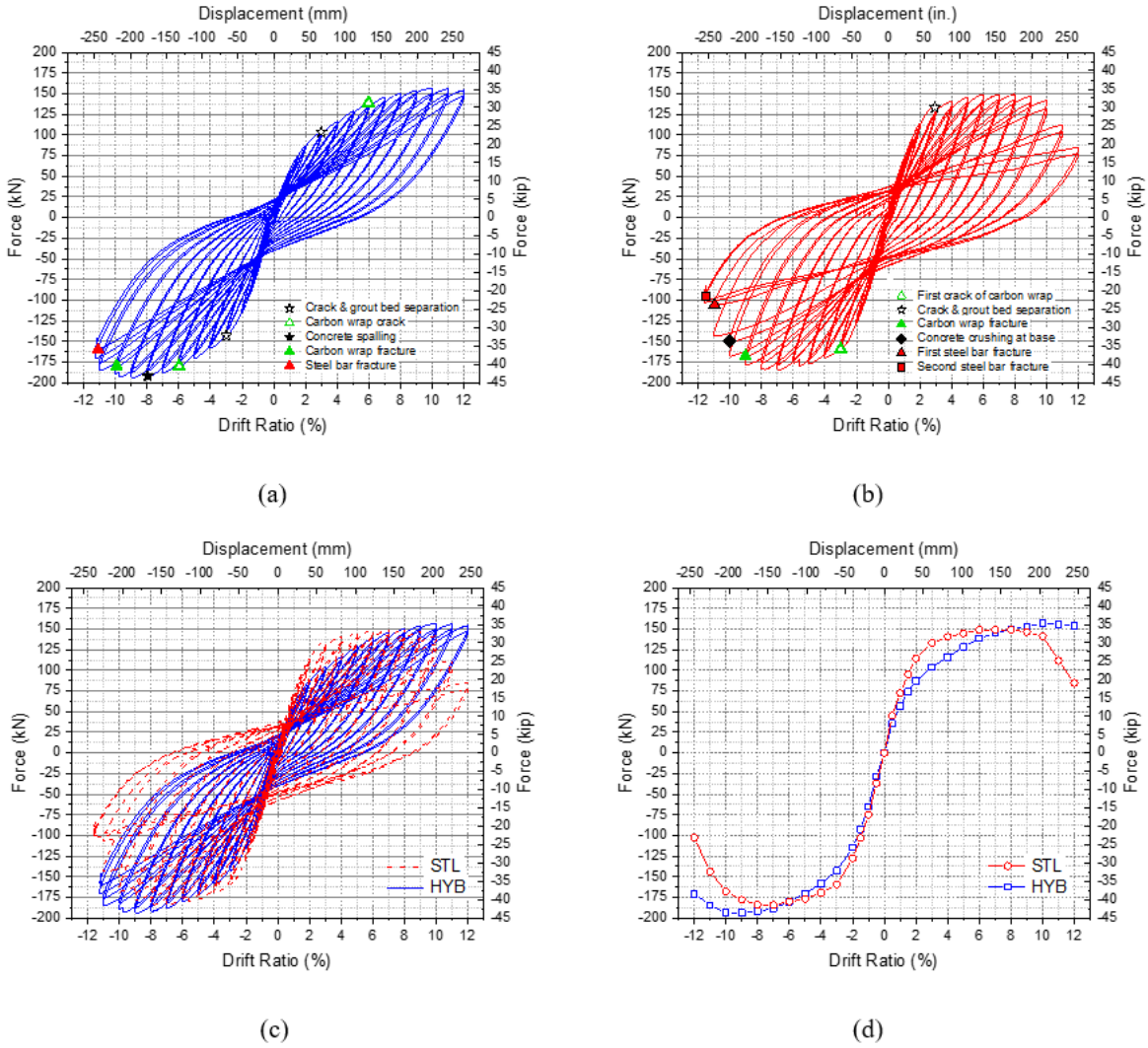

Figure 3.3 PT column hysteresis: (a) PT-HYB hysteresis; (b) PT-STL hysteresis; (c) PT-HYB vs PT-STL hysteretic comparison; and (d) PT-HYB vs PT-STL hysteretic envelopes

Figure 3.4 PT column damage: (a) PT-HYB column overall damage at 12% drift ratio;
(b) PT-HYB column steel bar fracture at 12.0% drift ratio;
(c) PT-STL column overall damage at 12% drift ratio; and
(d) PT-STL column steel bar fracture at 12.0% drift ratio

3.2.3 PT distribution force

Each PT bar was initially post-tensioned to a force of 191 kN. The fluctuation of PT forces during the tests is illustrated in **Figure 3.5**, depicting the relatively symmetrical behavior of the two PT bars for the PT-HYB and PT-STL columns. The slight asymmetry in the distribution of PT forces during the push and pull cycles is attributed to the progression of concrete damage in the columns. At a 3.0% drift ratio, the post-tensioning forces experienced a marginal decrease of 7% relative to their initial values, demonstrating good performance. However, severe concrete damage above the CFRP wrap was observed in the PT-HYB column at a 10.0% drift ratio, resulting in a substantial 70% decrease in the initial PT force. In contrast, the PT-STL column exhibited no concrete damage above the CFRP wrap, resulting in a lower decrease of 56% of the initial PT force at the end of the 10% drift ratio.

Notably, the PT bars are designed to withstand a yield capacity of 454 kN. During the PT-HYB test, the highest recorded force reached 398 kN, corresponding to 88% of the yield limit. In the PT-STL test, the highest recorded force was 413 kN, equivalent to 91% of the yield limit. This indicates that the PT bars did not yield during the tests, and there was no evidence of permanent deformation after the PT bars were removed.

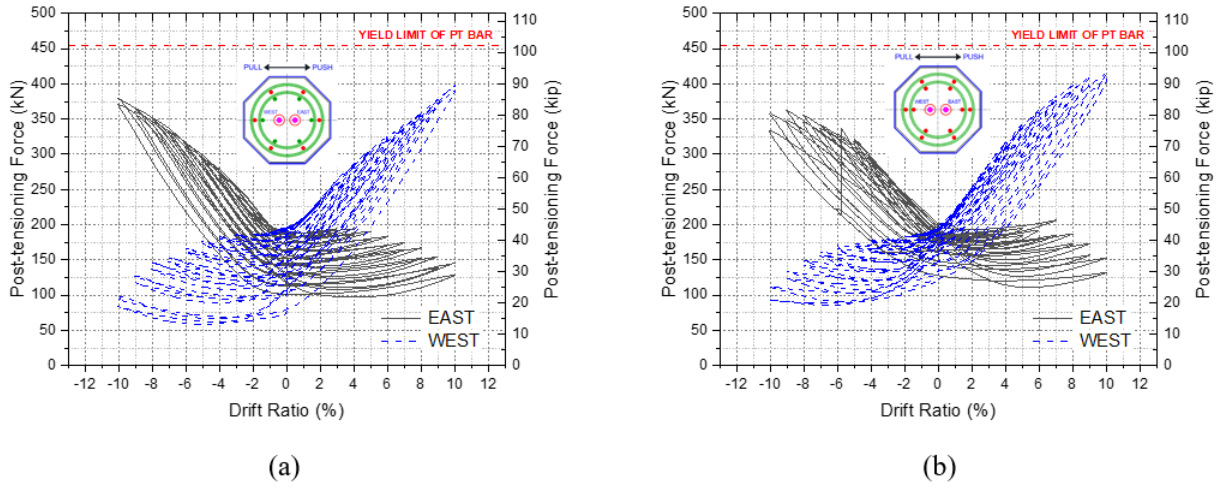

Figure 3.5 PT force distribution: (a) PT-HYB column; and (b) PT-STL column

4. TEST RESULTS

4.1 Non-PT Specimens

4.1.1 Residual displacement

Residual displacement, which denotes the remaining displacement within a bridge column after removing external forces, can significantly influence a bridge's overall performance and resilience following an earthquake. GFRP bars, owing to their linear elastic material characteristics, exhibit minimal residual displacement until GFRP fracture occurs. GFRP bars can be effectively utilized in columns to enhance self-centering capabilities and mitigate residual displacements by leveraging the advantageous yielding properties of traditional reinforcing steel bars. The hybrid (HYB) configuration combines both materials to improve self-centering and create a ductile column.

Figure 4.1(a) illustrates the residual displacement of the HYB column, while **Figure 4.1(b)** showcases the same for the STL column. Including double layers of GFRP spirals contributes to self-centering by enhancing the elastic lateral restraint on the column's concrete core, enabling the column to undergo substantial deformation. The hybrid column (HYB) further enhances self-centering by incorporating six GFRP longitudinal bars. Notably, GFRP bars exhibit reversible deformation characteristics, preserving their original shape and stiffness after removing the applied load.

At a 3.0% drift ratio, the average residual displacement for the HYB column measures 9 mm, whereas at a 6.0% drift ratio, the residual displacement increases to 37 mm. The STL column exhibits an average residual displacement of 13 mm at a 3.0% drift ratio, which escalates to 65 mm at a 6.0% drift ratio. It is important to note that both columns meet the allowable residual displacement limits specified under AASHTO LRFD Bridge Design Specifications at a 3.0% drift ratio. These limits are defined for Service Level I, intended for regular traffic, which specifies a threshold of 13 mm or 1.0% of the column height, whichever is smaller.

Replacing steel with GFRP bars in the inner layer of longitudinal reinforcement leads to a noteworthy reduction in residual displacement. This reduction amounts to 33% at a 3.0% drift ratio and increases to 43% at a 6.0% drift ratio, as depicted in **Figure 4.1(c)**. It is worth mentioning that the fracture of the longitudinal GFRP bars in compression during the pull cycle at the 9.0% drift ratio results in a noticeable increase in the residual displacement of the hybrid column. Nevertheless, this occurrence does not disrupt the residual displacement performance of the east side of the HYB column until the conclusion of the test, as presented in **Figure 4.1(c)**.

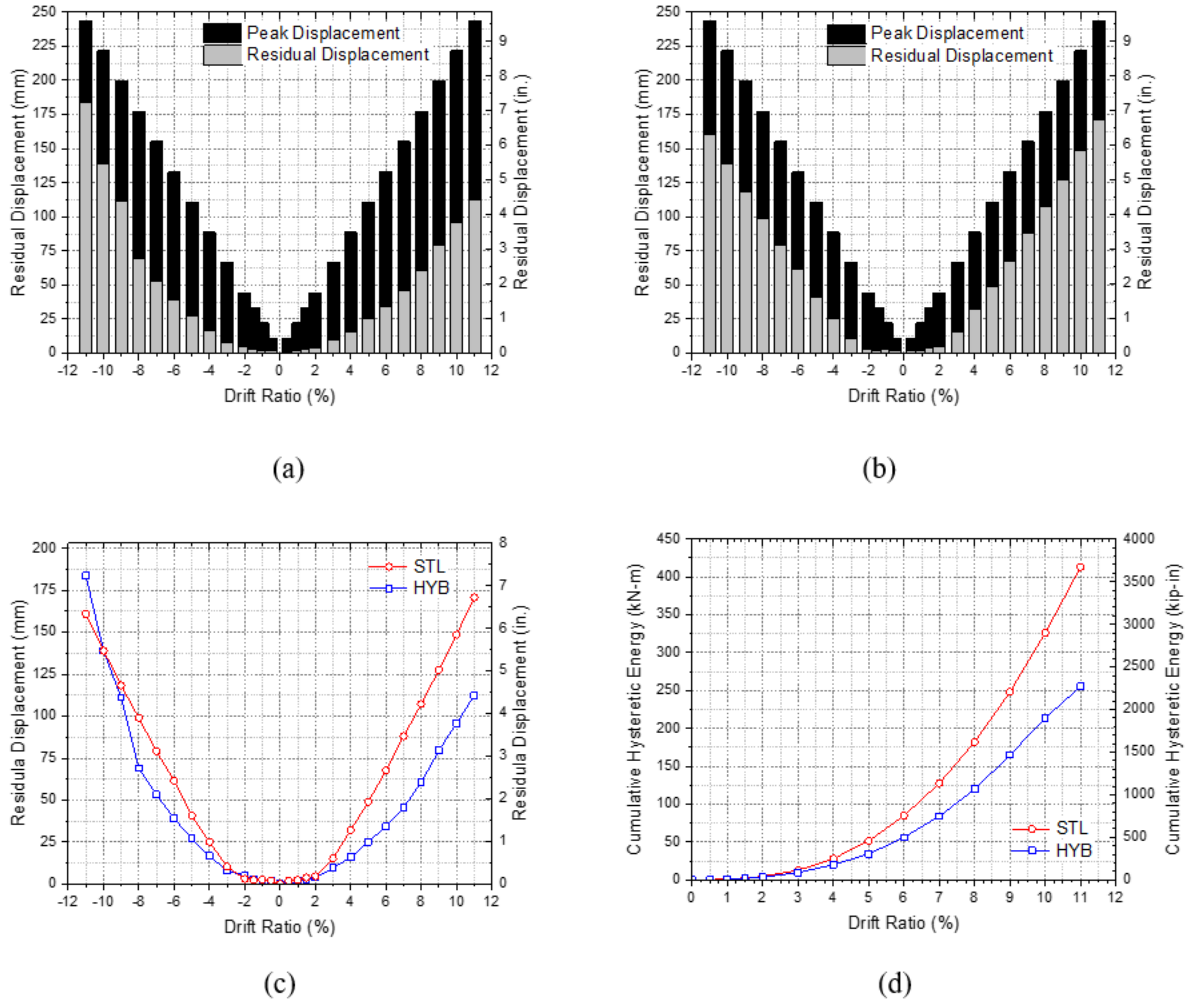

Figure 4.1 Non-PT hysteretic performance: (a) residual displacement of HYB column; (b) residual displacement of STL column; (c) comparison of residual displacement; (d) cumulative hysteric energy

4.1.2 Displacement ductility and hysteretic energy

Displacement ductility for each column was determined by applying equal energy principles to an idealized elastoplastic system. The effective yield displacement was estimated based on the intersection of the idealized elastoplastic curve with the average backbone curve at a force equivalent to 70% of the effective yield force. The ultimate displacement was defined as the point at which a 20% reduction in lateral load capacity occurred. The calculated displacement ductility was 4.0 for the HYB column and 5.5 for the STL column.

Figure 3.1(d) illustrates the cyclic force-displacement envelope for both tests. The HYB column exhibits a gradual strength increase, maintained until the compressive fracture of a GFRP reinforcing bar at a 9.0% drift ratio. In contrast, the STL specimen demonstrates a more rapid strength increase, reaching a plateau at a 3.0% drift ratio. Notably, the HYB column experiences GFRP bar fracture in compression at the 9.0% drift ratio. In comparison, the STL column experiences tensile fracture of longitudinal steel bars due to low-cycle fatigue at an 11.0% drift ratio. Both columns display localized fractures in two outer GFRP spiral turns near the column-to-footing interface. Grouted duct connections enhance ductility by facilitating plastic deformation and energy dissipation through increased confinement and lateral support

of the reinforcing bars. Additionally, these connections provide a mechanism for load transfer, thereby improving overall structural stability.

The cumulative hysteretic energy is presented in **Figure 4.1(d)**; up to a 3.0% drift ratio, both specimens exhibited similar energy dissipation behavior. Subsequently, energy dissipation increased for the STL column compared with the HYB column. At the 6.0% and 11.0% drift ratios, the STL column dissipated 52% and 62% more cumulative hysteretic energy, respectively. This difference in energy dissipation is attributed to the permanent deformation experienced by the steel longitudinal bars after yielding. In contrast, the GFRP bars maintained their linear elastic behavior until bar fracture.

4.2 PT Specimens

4.2.1 Residual displacement

Figure 4.2(a) illustrates the observed residual displacement in the PT-HYB column, while **Figure 4.2(b)** displays the residual displacement in the PT-STL column. A double layer of GFRP spirals contributes to self-centering by providing increased elastic lateral support to the concrete core. In the PT-HYB column, apart from the self-centering effect facilitated by the all-threaded post-tensioning rods, an additional self-centering effect is attributed to the six GFRP longitudinal bars. The strains in the two post-tensioning rods remain within the elastic range. At the same time, the GFRP bars undergo elastic deformation without fracturing and retain their original shape and stiffness after removal of the load. At a 3.0% drift ratio, the average residual displacement for the PT-HYB column is 6 mm; at a 6.0% drift ratio, it amounts to 23 mm. In the case of the all-steel longitudinal PT-STL column, the average residual displacement at a 3.0% drift ratio is 8 mm, and it increases to 48 mm at a 6.0% drift ratio. According to the AASHTO LRFD Bridge Design Specifications, both columns meet the allowable residual displacement criteria for Service Level I. This specification prescribes a maximum of 13 mm or 1.0% of the column height, whichever is smaller, at a drift ratio of 3.0%. Replacing the mild steel longitudinal bars with GFRP bars in the inner layer of reinforcement results in a 36% reduction in residual displacement at a 3.0% drift ratio and a 46% reduction at a 6.0% drift ratio, as depicted in **Figure 4.2(c)**. Furthermore, GFRP longitudinal bars lead to a further decrease in residual displacement as the drift ratio increases.

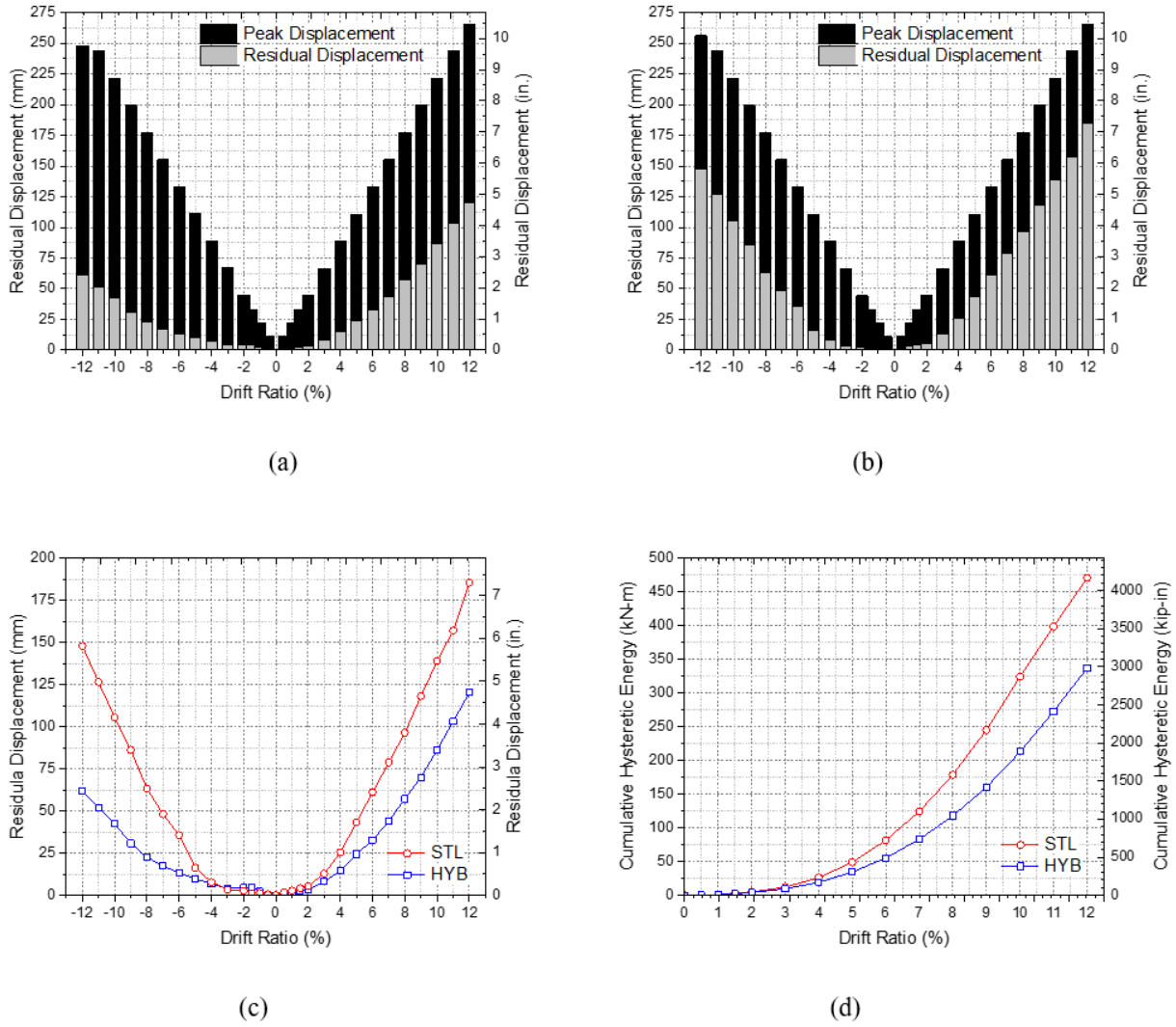

Figure 4.2 Hysteretic performance: (a) residual displacement of PT-HYB column; (b) residual displacement of PT-STL column; (c) PT-HYB vs PT-STL comparison of residual displacement; (d) PT-HYB vs PT-STL cumulative hysteric energy

4.2.2 Hysteretic energy

Figure 4.2(d) presents the cumulative hysteretic energy dissipation. Both specimens demonstrated comparable levels of hysteretic energy dissipation up to a 3.0% drift ratio. However, when we compare the PT-HYB column to the PT-STL column, the latter dissipated 47% more cumulative hysteretic energy at the 6.0% drift ratio and 40% more at the 12.0% drift ratio, which marks the end of the test. This difference in performance can be attributed to the fact that the steel longitudinal bars underwent permanent deformation after reaching their yield point. In contrast, the GFRP bars maintained their linear elastic behavior throughout the test.

5. SUMMARY AND CONCLUSIONS

5.1 Summary

Research on seismic evaluation of a grouted duct connection of column-to-footing or column-to-cap beam in ABCs was developed and presented. Four columns were reinforced with conventional steel, GFRP bars, and GFRP spiral. Two of the columns were post-tensioned using high-strength threaded bars to promote the effect of self-centering.

In the first phase of this study, eight pull-out specimen tests were performed to investigate the minimum embedded length of M19 GFRP rebars in 76-mm diameter UHPG ducts. Those tests aimed to identify the failure modes of embedded M19 GFRP bars in grouted ducts. Several modes of failure are possible in grout-filled duct connections: (1) bar fracture, (2) bar pull-out caused by bond failure, (3) grout pull-out from the duct, and (4) duct pull-out by either failure of the bond between concrete surrounding the duct and the duct or conical failure of concrete. This type of connection has two critical bond surfaces: the bar-grout interface and the grout-duct-concrete interface. With proper design and consideration, grouted duct connections for ABC bridges have been used in both non-seismic and seismic regions. The targeted failure is bar fracture, not pull-out of bar, grout, or ducts.

The test matrix of the second phase of this study provided a combination of GFRP confinement, hybrid longitudinal systems, and self-centering capability by post-tensioning in grouted duct connections. This combination exhibits several improvements over traditional methods: corrosion resistance for concrete cores to continue providing effective confinement, the capability to reduce permanent residual displacement after an earthquake, and material and design readiness for grouted duct connection type in ABCs. Each test setup exhibited varying loading capacity, displacement properties, energy dissipation capability, and self-centering ability. Four specimens were constructed for testing; each included a column and a footing. These specimens were categorized into post-tensioning and non-post-tensioning groups. All columns contained two layers of longitudinal reinforcement and shared the same outer layer of conventional longitudinal steel bars. This layer of steel reinforcement allows higher strain development while yielding, promoting higher ductility and preventing abrupt failure. The inner layer of longitudinal reinforcement was steel or GFRP bars, which classified the column as a hybrid or an all-steel system. Double-layered GFRP spirals were adapted for all columns for enhanced corrosion resistance. Two all-threaded PT bars were provided after specimen assembly through embedded PVC pipes for the two columns of the PT group. Along with the elastic properties of GFRP reinforcement, the PT bars contribute to the system's re-centering capability.

This research is unique because, based on the current state of research, there are remaining knowledge gaps on the seismic response of ABC hybrid reinforced columns using grouted duct connections with self-centering post-tensioning. They are as follows: no information is available for the development length of GFRP bars in grouted ducts; only a few references on the seismic performance of precast GFRP reinforced columns are available; no information on the seismic performance of hybrid columns is available; no information on the seismic performance of hybrid columns incorporating PT for self-centering effect is available; finally, no information on the seismic performance of steel/hybrid columns confined with double layers of GFRP spirals is available.

5.2 Conclusions

In the study's first phase, eight pull-out tests were conducted to identify the desired embedment length to prevent the pull-out failure. Two distinct failure modes were observed for the eight conducted tests: bar pull-out and bar fracture. Bar pull-out failures with an embedded length of 8db were noted in both tests.

In contrast, for lengths of 10db, 12db, and 14db, the predominant failure mode observed was bar fracture under tension. Therefore, 10 times the bar diameter of M19 GFRP bars was sufficient to achieve the bar fracture as the failure mode, which was used to configure the column assemblies.

Half-scale bridge column-to-footing and column-to-cap beam specimens were tested under cyclic loading to failure in the study's second phase. The experimental test data offers qualitative and quantitative insights into the behavior of the bridge columns when subjected to quasi-static cyclic loads. The conclusions drawn from this second phase of the study are as follows:

- All specimens behaved satisfactorily up to a high drift ratio of 11.0% (non-PT columns) and 12.0% drift ratio (PT columns). All four columns experienced longitudinal steel bar fractures; this shows a satisfactory performance of the high-strength grout in bonding the longitudinal bars in grouted ducts without bar pull-out.

5.2.1 Non-PT specimens

- Both columns experienced tensile fractures of their longitudinal steel bars due to low-cycle fatigue and outer GFRP spiral fractures caused by buckling of the longitudinal steel bars. In the case of the hybrid column, GFRP longitudinal bars experienced a compressive fracture. Notably, the inner GFRP spiral in both columns remained intact. The HYB and STL columns exhibited ductile behavior, with the high-strength grout effectively bonding the longitudinal reinforcement without any pull-out failures.
- The performance of the columns was significantly influenced by their flexural behavior and the development of a plastic hinge at the column base. The HYB column achieved a lateral capacity of 120 kN, while the STL column reached 130 kN. Both columns displayed stable hysteresis behavior until an 11% drift ratio, indicating that combining GFRP and steel vertical bars is viable. The displacement ductility for HYB was determined to be 4.0, whereas STL exhibited a value of 5.5. Interestingly, the HYB column exhibited a gradual strength increase that continued until the reinforcement fractured. In contrast, the STL column experienced rapid strength growth before reaching a plateau at the 3.0% drift ratio.
- The presence of a double layer of GFRP spirals contributed to the effective confinement of the concrete core, ensuring elastic performance. To account for the relatively low elastic modulus of GFRP, it is advisable to use a higher spiral ratio than conventional steel spirals. Replacing steel vertical bars in the inner layer of longitudinal reinforcement with six GFRP bars significantly improved self-centering performance, resulting in a 33% reduction in residual displacement at a 3.0% drift ratio and a 43% reduction at a 6.0% drift ratio.
- Compared with the HYB column, the STL column exhibited a 52% higher cumulative hysteretic energy dissipation at the 6.0% drift ratio and a 62% higher dissipation at the 11.0% drift ratio. This disparity can be attributed to the permanent deformation of the steel longitudinal bars after yielding in the STL column, while the GFRP bars maintained their linear elastic behavior throughout.

5.2.2 PT specimens

- The PT-HYB and PT-STL specimens exhibited satisfactory performance up to a high 11.0% drift ratio. In both columns, longitudinal steel bar fractures and CFRP wrap fractures were observed, highlighting the adequate bonding of longitudinal bars within grouted ducts with no bar pull-out. Notably, while the PT-STL column experienced the fracture of two longitudinal steel bars in tension due to low-cycle fatigue, the PT-HYB column had one steel bar fracture under similar conditions.

- There were no observed failures in the GFRP spirals, whether inner or outer, for either the PT-HYB or PT-STL columns. Additionally, the longitudinal GFRP bars in the PT-HYB column did not experience any fractures. The CFRP wrap, however, fractured in tension due to the increased dilation of the concrete core near the column-to-footing interface. It is recommended to incorporate vertical CFRP strips and the CFRP wrap to mitigate this. This can reduce the occurrence and size of horizontal cracks and delay CFRP fracture.
- The cyclic performance of the columns was primarily influenced by flexural behavior and the formation of a plastic hinge. At lower drift ratios, the CFRP wrap provided stiffness over the jacketed segment of the columns, shifting concrete damage to the segment above the wrap. However, as the CFRP wrap developed cracks and fractures, reduced confinement led to forming the plastic hinge near the column base, close to the column-to-footing interface, resulting in concrete crushing.
- The lateral capacity of both the PT-HYB and PT-STL columns was comparable. Both columns exhibited stable hysteresis behavior until the 11.0% drift ratio, indicating the effectiveness of combining GFRP and steel longitudinal bars with post-tensioning. The PT-HYB column displayed a gradual and sustained increase in lateral load. In contrast, the PT-STL column exhibited a rapid increase in lateral load followed by a yield plateau, which occurred at a 6.0% drift ratio.
- All post-tensioning bars were initially tensioned to a force equivalent to 42% of their yield strength. At a 3.0% drift ratio, both columns experienced only a 7% reduction in post-tensioning force compared with the initial value. However, the PT-HYB column exhibited concrete deterioration above the CFRP wrap, leading to a 70% reduction in the initial post-tensioning force at a 10.0% drift ratio. In contrast, the PT-STL column had no concrete spalling above the CFRP wrap, resulting in a 56% reduction in the initial post-tensioning force at a 10% drift ratio. Notably, throughout the PT-HYB and PT-STL tests, the post-tensioning bars did not yield.
- Including a double layer of GFRP spirals effectively confined the concrete core. Substituting longitudinal mild steel bars in the inner layer with GFRP bars improved self-centering performance. Comparatively, the PT-HYB column exhibited a 36% reduction in residual displacement at a 3.0% drift ratio and a 46% reduction at a 6.0% drift ratio in contrast with the PT-STL column.
- The PT-STL column demonstrated more excellent hysteretic energy dissipation than the PT-HYB column, with a 47% increase in cumulative hysteretic energy dissipation at a 6.0% drift ratio and a 40% increase at a 12.0% drift ratio.

5.3 Recommendations for Further Research

Future research efforts should prioritize a more in-depth investigation into the performance of GFRP bars and GFRP spiral regarding self-centering contribution, in addition to high-strength PT bars. Further experimental tests involving varying combinations of axial loads, initial post-tensioning forces, number of longitudinal bars, and bridge column dimensions should be conducted to enhance the self-centering capabilities of the specimens, aiming to minimize residual drift and enhance energy dissipation. The CFRP external wrapping witnessed horizontal cracks, indicating that vertical layers of CFRP wraps will offer better protection and overall performance of CFRP wrapping.

Computational models can be constructed for each testing case and validated by recorded experiment data. Concentrated plasticity models apply calibration of an advanced hysteretic rule to effectively simulate a component's strength and stiffness reduction response under cyclic loading. This method has gained popularity in seismic design and analysis due to its simplicity; therefore, it is a proper initial approach for the experimental data. It is also crucial to develop streamlined design guidelines to assist engineers in designing precast, post-tensioned bridge columns featuring these unique connections.

6. REFERENCES

AASHTO Guide Specifications for LRFD Seismic Bridge Design, Washington D.C., 2011.

AASHTO LRFD Bridge Design Specifications, Washington, D.C., 2012.

Abdallah E., Amr, and El-Salakawy, Ehab (2021). "Confinement Properties of GFRP-Reinforced Concrete Circular Columns under Simulated Seismic Loading." *J. Compos. Constr.* 25(2): 04020088.

Abdallah E., Amr, and El-Salakawy, Ehab (2021). "Seismic Behavior of High-Strength Concrete Circular Columns Reinforced with Glass Fiber-Reinforced Polymer Bars." *ACI Structural Journal*, V. 118, No. 5: 10.14359/51732831.

Abdallah E., Amr, and El-Salakawy, Ehab (2022). "Seismic Performance of GFRP-RC Circular Columns with Different Aspect Ratios and Concrete Strengths." *Engineering Structures* 257: 114092.

ACI Committee 318, Building Code Requirements for Structural Concrete (ACI 318-08) and Commentary, Farmington Hills: American Concrete Institute, 2008.

ACI PRC-440.1-15 Guide for the Design and Construction of Structural Concrete Reinforced with Fiber-Reinforced Polymer Bars. American Concrete Institute, 2015.

ACI PRC-440-07 Report on Fiber-Reinforced Polymer (FRP) Reinforcement for Concrete Structures. American Concrete Institute, 2007.

Ali M. A., and El-Salakawy, E. (2016). "Seismic Performance of GFRP-Reinforced Concrete Rectangular Columns." *J. Compos. Constr*. 20(3): 04015074.

Ameli, M.J., et al. (2014). "Seismic evaluation of grouted splice sleeve connections for precast R.C. bridge piers in ABC." Report UT-14.09, Utah Department of Transportation, Salt Lake City, UT.

Ameli, M.J., Parks, J.E., Brown, D.N., and Pantelides, C.P. (2015). "Seismic evaluation of grouted splice sleeve connections for reinforced precast concrete column-to-cap beam joints in accelerated bridge construction." *PCI Journal*, 80–103.

Ameli, M.J., et al. (2016). "Seismic column-to-footing connections using grouted splice sleeves." *ACI Structural J*., 113(5), 1021–1030.

Arafa Ahmed, Chaallal Omar, and Benmokrane Brahim (2022). "Effects of Axial Load on Seismic Behavior of Glass Fiber Reinforced Polymer-Reinforced Concrete Columns: A Numerical Study." *ACI Structural Journal*, V. 119, No. 3: 10.14359/51734434.

ASTM C 31 (2019). Standard Practice for Making and Curing Concrete Test Specimens in the Field. American Society for Testing and Materials. West Conshohocken, PA.

Billington, S.L., and Yoon, J.K. (2004). "Cyclic Response of Unbonded Post-tensioned Precast Columns with Ductile Fiber-Reinforced Concrete." *Journal of Bridge Engineering* 9 (4): 353–63. https://doi.org/10.1061/(ASCE)1084-0702(2004)9:4(353).

California Department of Transportation (Caltrans). Seismic design criteria, Version 1.7. Sacramento, CA; 2013.

Chang, G., and Mander, J. (1994). "Seismic Energy Based Fatigue Damage Analysis of Bridge Columns: Part I – Evaluation of Seismic Capacity." NCEER Technical Report 94-0006.

Cheng, C.T. (2008). "Shaking Table Tests of a Self-Centering Designed Bridge Substructure." *Engineering Structures* 30 (12): 3426–33. https://doi.org/10.1016/j.engstruct.2008.05.017.

Culmo, M.P. (2011). "Accelerated Bridge Construction: Experience in Design, Fabrication and Erection of Prefabricated Bridge Elements and Systems," no. 100: 1–347.

Elchalakani, M., and Ma, G. (2017). “Tests of Glass Fibre Reinforced Polymer Rectangular Concrete Columns Subjected to Concentric and Eccentric Axial Loading.” *Engineering Structures*, 151, 93-104. doi:10.1016/j.engstruct.2017.08.023.

Elshamandy G. M., Farghaly S. A., and Benmokrane, B. (2018). “Experimental Behavior of Glass Fiber-Reinforced Polymer Reinforced Concrete Columns under Lateral Cyclic Load.” *ACI Structural Journal*, V. 115, No. 2: 10.14359/51700985.

Hadhood, A., Mohamed, H. M., Ghrib, F., and Benmokrane, B. (2017). “Efficiency of Glass-Fiber Reinforced-Polymer (GFRP) Discrete Hoops and Bars in Concrete Columns under Combined Axial and Flexural Loads.” *Composites Part B: Engineering*, 114, 223-236. doi:10.1016/j.compositesb.2017.01.063.

Hadi, M. N. S., Karim, H., and Sheikh, M. N. (2016). “Experimental Investigations on Circular Concrete Columns Reinforced with GFRP Bars and Helices under Different Loading Conditions.” *Journal of Composites for Construction*, 20(4) doi:10.1061/(ASCE)CC.1943-5614.0000670.

Hales, T., Pantelides, C. P., and Reaveeley, L. (2016). “Experimental Evaluation of Slender High-Strength Concrete Columns with GFRP and Hybrid Reinforcement.” *Journal of Composites for Construction*. 20. 04016050. 10.1061/(ASCE)CC.1943-5614.0000709.

Hales, Thomas A., et al. (2017). “Analysis-Oriented Stress-Strain Model for Concrete Confined with Fiber-Reinforced Polymer Spirals.” *ACI Structural Journal*, vol. 114, no. 5, pp. 1263+.

Hamzeh Layane, Hassanein Ahmed, and Galal Khaled (2020). “Numerical Study on the Seismic Response of GFRP and Steel Reinforced Masonry Shear Walls with Boundary Elements.” *Structures* 28 (2020) 1946–1964.

Jia Junfeng, Wei Bo, Bai Yulei, Wu Suiwen, Zhang Kaidi, and Guo Yang (2021). “Seismic Performance of Precast Segmental Bridge Columns Reinforced with Both Stainless-Steel Bars and GFRP Bars.” *Journal of Bridge Engineering*: 10.1061/(ASCE)BE.1943-5592.0001810.

Karim, H., Sheikh, M. N., and Hadi, M. N. S. (2016). “Axial Load-Axial Deformation Behavior of Circular Concrete Columns Reinforced with GFRP Bars and Helices.” *Construction and Building Materials*, 112, 1147-1157. doi:10.1016/j.conbuildmat.2016.02.219.

Kawashima, K. (2019). “The 1996 Japanese Seismic Design Specifications of Highway Bridges and the Performance Based Design.” *Seismic Design Methodologies for the Next Generation of Codes*, 371–82. https://doi.org/10.1201/9780203740019-33.

Kharal Zahra and Sheikh A. Shamim (2018). “Seismic Performance of Square Concrete Columns Confined with Glass Fiber–Reinforced Polymer Ties.” *Journal of Composites for Construction*, ASCE: 10.1061/(ASCE)CC.1943-5614.0000884.

Kharal Zahra and Sheikh A. Shamim (2020a). “Seismic Behavior of Square and Circular Concrete Columns with GFRP Reinforcement.” *Journal of Composites for Construction*: 10.1061/(ASCE)CC.1943-5614.0000988.

Kharal Zahra and Sheikh A. Shamim (2020b). “Seismic Behavior of Square and Circular Concrete Columns with GFRP Reinforcement.” *J. Compos. Constr*. 24(1): 04019059.

Kharal Zahra, Carrette K. Jordan, and Sheikh A. Shamim (2021). “Large Concrete Columns Internally Reinforced with GFRP Spirals Subjected to Seismic Loads.” *Journal of Composites for Construction*, ASCE: 10.1061/(ASCE)CC.1943-5614.0001121.

Liu James and Sheikh A. Shamim (2013). “Fiber-Reinforced Polymer-Confined Circular Columns under Simulated Seismic Loads.” *ACI Structural Journal*, V. 110, No. 6: S-2011-341.R1.

Mander, J. B., et al. (1988). “Theoretical stress-strain model for confined concrete.” *J. Struct. Eng*., 10.1061/(ASCE) 0733-9445(1988)114:8(1804), 1804-1826.

Maranan, G. B., Manalo, A. C., Benmokrane, B., Karunasena, W., and Mendis, P. (2016). “Behavior of Concentrically Loaded Geopolymer-Concrete Circular Columns Reinforced Longitudinally and Transversely with GFRP Bars.” *Engineering Structures*, 117, 422-436. doi:10.1016/j.engstruct.2016.03.036.

Matsumoto, E. (2009). “Emulative Precast Bent Cap Connections for Seismic Regions: Grouted Duct and Cap Pocket Test Results, Design and Construction Specifications, Design Examples, and Connection Details.” Report No. ECS-CSUS-2009-05. California State University, Sacramento.

M. L. Marsh, M. Wernly, B. E. Garett, J. F. Stanton, M. O. Eberhard., and M. D. Weinert (2011). “Application of Accelerated Bridge Construction Connections in Moderate-to-High Seismic Regions,” NCHRP, Washington, D.C.

Mohamed, H. M., Afifi, M. Z., and Benmokrane, B. (2014). “Performance Evaluation of Concrete Columns Reinforced Longitudinally with FRP Bars and Confined with FRP Hoops and Spirals under Axial Load.” *Journal of Bridge Engineering*, 19(7) doi:10.1061/(ASCE)BE.1943-5592.0000590.

Naqvi Syed, Mahmoud Karam, and El-Salakawy Ehab (2017). “Effect of Axial Load and Steel Fibers on the Seismic Behavior of Lap-Spliced Glass Fiber Reinforced Polymer-Reinforced Concrete Rectangular Columns.” *Engineering Structures* 134: 376–389.

Ou, Y. C., Wang, P. H., Tsai, M. S., Chang, K. C., and Lee, G. C. (2010). “Large-Scale Experimental Study of Precast Segmental Unbonded Post-tensioned Concrete Bridge Columns for Seismic Regions.” *Journal of Structural Engineering*, 136(3), pp. 255–264.

Pang, J. B. K., Eberhard, M. O., and Stanton, J. F. (2010). “Large-Bar Connection for Precast Bridge Bents in Seismic Regions.” *Journal of Bridge Engineering*, 15(3), pp. 231–239.

Palermo, A., Pampanin, S., and Marriott, D. (2007). “Design, Modeling, and Experimental Response of Seismic Resistant Bridge Piers with Posttensioned Dissipating Connections.” *Journal of Structural Engineering* 133 (11): 1648–61.

Pantelides, C.P., Gibbons, M., and Reaveley, L.D. (2013). “Axial Load Behavior of Concrete Columns Confined with GFRP Spirals.” *Journal of Composites for Construction*, 17, 305-313.

Park, R. (2011). “ABC in Utah, Accelerated Bridge Construction: Research, Design, and Practice Workshop.” Presented at the 90th Annual Meeting of the Transportation Research Board, Washington, DC.

PCI Design Handbook—Precast and Prestressed Concrete. (2004). (6th ed.) Precast/Prestressed Concrete Institute, Chicago, IL.

Restrepo, J., Matsumoto, E., and Tobolski, M. (2011). “NCHRP Report 681: Development of Precast Bent Cap Systems for Seismic Regions.” Transportation Research Board of the National Academies, Washington, DC.

Sankholkar, P., Pantelides, C. P., and Hales, T. (2018). “Confinement Model for Concrete Columns Reinforced with GFRP Spirals.” *Journal of Composites for Construction*. 22. 10.1061/(ASCE)CC.1943-5614.0000843.

Tavassoli Arjang, Liu James, and Sheikh Shamim (2015). “Glass Fiber-Reinforced Polymer-Reinforced Circular Columns under Simulated Seismic Loads.” *ACI Structural Journal*, V. 112, No. 1: 10.14359/51687227.

Tazarv, M., and Saiidi, M. S. (2013). “Emulative Moment-Resistant RC Bridge Column-Footing Connection for Accelerated Bridge Construction in High Seismic Zone,” in Seventh National Seismic Conference on Bridges & Highways, Oakland.

Tazarv, M., and Saiidi, M.S. “Next generation of bridge columns for accelerated bridge construction in high seismic zones.” Report No. CCEER 14-06, Center for Civil Engineering Earthquake Research, Department of Civil and Environmental Engineering, Univ. of Nevada, Reno, Reno, NV, 2014.

Tazarv, M., and Saiidi, M.S. (2016). “Low-Damage Precast Columns for Accelerated Bridge Construction in High Seismic Zones.” *Journal of Bridge Engineering* 21 (3): 04015056. https://doi.org/10.1061/(ASCE)be.1943-5592.0000806.

Tazarv, M., and Saiidi, M.S., “UNR-Caltrans Research Projects,” UNR-Caltrans, 2014. [Online]. Available: http://wolfweb.unr.edu/homepage/saiidi/caltrans/NextGen/PDFs/HCSPreliminaryResults214.pdf.

Teng J. G., Lam L., Lin G., Lu J. Y., and Xiao, Q. G. (2015). “Numerical Simulation of FRP-Jacketed RC Columns Subjected to Cyclic and Seismic Loading.” *Journal of Composites for Construction*: 10.1061/(ASCE)CC.1943-5614.0000584.

Wright, John, and Pantelides, Chris. (2021). “Axial Compression Capacity of Concrete Columns Reinforced with Corrosion-Resistant Metallic Reinforcement.” 10.21203/rs.3.rs-144431/v2.

Zadeh Jawaheri Hany and Nanni Antonio (2012). “Design of R.C. Columns Using Glass FRP Reinforcement.” *Journal of Composites for Construction*, Vol. 17, No. 3: 10.1061/(ASCE)CC.1943-5614.0000354.